

1 ~~On~~ Warm and Moist Air Intrusions into Winter Arctic: A Lagrangian view on the near-surface energy
2 budgets

3 Cheng You¹, Michael Tjernström¹, Abhay Devasthale²

4 ¹Department of Meteorology & Bolin Centre for Climate Research, Stockholm University, Stockholm, Sweden.

5 ²Remote Sensing Unit, Research and Development Department, Swedish Meteorological and Hydrological
6 Institute, Norrköping, Sweden.

7
8 Correspondence to: Cheng You (cheng.you@misu.su.se)

9 **Abstract.** In this study, warm and moist air intrusions (WaMAI) over the Arctic Ocean sectors of Barents, Kara,
10 Laptev, East Siberian, Chukchi and Beaufort Seas in recent 40 winters (from 1979 to 2018) are identified from
11 ERA5 reanalysis using both Eulerian and Lagrangian views. The analysis shows that WaMAIs, fuelled by Arctic
12 blockings, causes a relative surface warming and hence a sea ice reduction by exerting positive anomalies of net
13 thermal irradiances and turbulent fluxes to the surface. Over Arctic Ocean sectors with land-locked sea ice in
14 winter, such as Laptev, East Siberian, Chukchi and Beaufort Seas, total surface energy budget is dominated by
15 net thermal irradiance. From a Lagrangian perspective, total water path (TWP) increases linearly with the
16 downstream distance from the sea ice edge over the completely ice-covered sectors, inducing almost linearly
17 increasing net thermal irradiance and total surface energy-budget. However, over the Barents Sea, with an open
18 ocean to the south, total net surface energy-budget is dominated by the surface turbulent flux. With the energy in
19 the warm-and-moist air continuously transported to the surface, net surface turbulent flux gradually decreases
20 with distance, especially within the first 2 degrees north of the ice edge, inducing a decreasing but still positive
21 total surface energy budget. The boundary-layer energy-budget patterns over the Barents Sea can be categorized
22 into three classes: radiation-dominated, turbulence-dominated and turbulence-dominated with cold dome,
23 comprising about 52%, 40% and 8% of all WaMAIs, respectively. Statistically, turbulence-dominated cases with
24 or without cold dome occur along with one order of magnitude larger large-scale subsidence than the radiation-
25 dominated cases. For the turbulence-dominated category, larger turbulent fluxes are exerted to the surface,
26 probably because of stronger wind shear. In radiation-dominated WaMAIs, stratocumulus develops more strongly
27 and triggers intensive cloud-top radiative cooling and related buoyant mixing that extends from cloud top to the
28 surface, inducing a thicker well-mixed layer under the cloud. With the existence of cold dome, fewer liquid water
29 clouds were formed and less or even negative turbulent fluxes could reach the surface.

30 Keywords: Arctic climate, Stratocumulus, Trajectories, Warm and moist air intrusions

31 **1. Introduction**

32 ~~In recent decades, rapidly intensified Arctic warming has been observed (Cohen et al., 2014; Francis and Vavrus,~~
33 ~~2012; Graverson et al., 2008), which has become known as Arctic amplification (In recent decades, rapidly~~
34 ~~intensified Arctic warming has been observed (Cohen et al., 2014; Graverson et al., 2008a; Screen et al., 2018),~~
35 ~~which has become known as Arctic amplification (Serreze and Francis 2006). Accompanying this warming has~~
36 ~~been a dramatic melting of Arctic sea ice (Simmonds, 2015). Particularly over the Barents Sea, a rapid warming~~
37 ~~rate, as well as a remarkable sea ice decrease, is found, which may have impacts on the extreme cold winter in~~

38 Eurasia (Kim et al., 2014; Kim and Son, 2016; Mori et al., 2014; Overland et al., 2011; Petoukhov and Semenov,
39 2010; Tang et al., 2013).

40 ~~Arctic amplification is likely a consequence of many contributing processes and a detailed attribution to different
41 factors is yet to be performed.~~ Accompanying this warming has been a dramatic melting of Arctic sea ice (Screen
42 and Simmonds, 2010; Simmonds, 2015; Simmonds and Li, 2021). Particularly over the Barents Sea, a rapid
43 warming rate, as well as a remarkable sea ice decrease, is found, which may have impacts on the extreme cold
44 winters in Eurasia (Kim et al., 2014; Kim and Son, 2016; Li et al., 2021; Luo et al., 2019; Mori et al., 2014;
45 Overland et al., 2011; Petoukhov and Semenov, 2010; Rudeva and Simmonds, 2021; Tang et al., 2013).

46 ~~Arctic amplification is likely a consequence of many contributing processes and a detailed attribution to different
47 factors is yet to be performed.~~ The most commonly implied mechanism is the so-called albedo feedback, based
48 on the consideration that open water absorbs considerably more solar radiations than sea ice, which would
49 accelerate Arctic warming (Kim et al., 2019). ~~However, Arctic amplification is the strongest in winter, when the
50 sun is mostly absent and the albedo by definition plays no role at all. This suggests that atmospheric energy
51 transport by warm and moist intrusions (WaMAD) may play an important role for Arctic amplification, especially
52 in winter. The positive trend in number of winter WaMAIs can statistically explain a substantial part of the surface
53 air temperature and sea ice concentration trends in the Barents Sea (Woods and Caballero, 2016).~~ However,
54 ~~Arctic amplification is the strongest in winter, when the sun is mostly absent and the albedo by definition plays
55 no role at all. This suggests that atmospheric energy transport by warm and moist intrusions (WaMAI) may play
56 an important role for Arctic amplification, especially in winter. The positive trend in number of winter WaMAIs
57 can statistically explain a substantial part of the surface air temperature and sea-ice concentration trends in the
58 Barents Sea (Luo et al., 2017; Nygård et al., 2020; Woods and Caballero, 2016).~~

59 Most of these studies deal with winter and focus either on the dynamical mechanisms resulting in WaMAIs, or on
60 the effects of WaMAIs on the Arctic climate system conducted from an Eulerian perspective by retrieving
61 composite mean of WaMAIs properties (Liu et al., 2018), or calculating regressions between different metrics
62 (Gong and Luo, 2017). In recent years it has been increasingly argued that the concept of Lagrangian air mass
63 transformation is necessary for studying WaMAIs (~~Pithan et al. 2018, 2020; Komatsu et al. 2018, Tjernström et
64 al. 2019~~)(Ali and Pithan, 2020; Komatsu et al., 2018; Pithan et al., 2018). Trajectories have been utilized to study
65 ~~the origin and transport pathway of winter WaMAIs (Papritz et al., 2022), as well as the thermodynamic processes
66 along the trajectories (Papritz, 2020).~~ A method using trajectories to analyze WaMAIs from a Lagrangian
67 perspective was designed by You et al. (2020) and tested on a summer WaMAI event described in Tjernström et
68 al. (2015). This method was utilized to build a climatology of summer WaMAIs (You et al., 2021).

69 In this paper, we use this method to explore winter WaMAIs over several sectors of the Arctic Oceans: the Barents,
70 Kara, Laptev, East Siberian, Chukchi and Beaufort Seas. Over the Barents Sea, sea ice concentration is decreasing
71 and the near-surface atmosphere south of the ice edge is heated by comparatively warm open water. In contrast,
72 for the Laptev, East Siberian, Chukchi and Beaufort Seas, the ocean surface is almost completely frozen to the
73 coast and the insulation effect by sea ice suppresses heat transfer between ocean and atmosphere. We will attempt
74 understanding the distinctions between the ocean sector with open water and those with land-locked sea ice by
75 comparing surface and boundary-layer energy-~~budget~~budgets from both Eulerian and Lagrangian perspectives.

76 2. Data and method

77 2.1 Data

78 We use the latest reanalysis from European Centre for Medium-Range Weather Forecast (ECMWF), ERA5
79 (Hersbach et al., 2020) in this study. For the detection and Eulerian analysis of WaMAIs in recent 40 winters
80 (DJF from 1979 to 2018), we use the reanalysis dataset at a 6-hourly temporal and 0.75° horizontal resolution.
81 This includes the vertically integrated northward water vapor flux (f_w), sea ice concentration (SIC), 500-hPa
82 geopotential height (GH_{500}), 2m air temperature (T_{2m}), 850-hPa temperature (T_{850}), total water path (TWP),
83 liquid water path (LWP), ice water path (IWP) and precipitation rate (PRCP). For the Lagrangian analysis we also
84 use ERA5 3D wind field at a 6-hourly resolution for the calculations of air-mass trajectories ~~calculations~~ during
85 WaMAIs, in the same way as described in You et al. (2020, 2021). ~~For this we~~ We additionally ~~use~~ interpolate
86 energy-budget terms with forecast data from ERA5 at the higher temporal resolution (1-hourly). This includes
87 surface net solar (F_{sw}) and thermal (F_{lw}) irradiances, the surface sensible (F_{sh}) and latent heat fluxes (F_{lh}), as well
88 as the 1-hourly temperature tendencies due to different model physics extracted at model levels.

89 ~~Utilizing reanalysis introduces uncertainty, especially for the energy budget terms. Mean variables in a~~
90 ~~reanalysis are constrained by observations in the data assimilation. In situ observations over the central Arctic~~
91 ~~Ocean are sparse, especially in winter, and the loss of all visible wavelengths in passive remote sensing in winter~~
92 ~~makes the satellite products less trustworthy. However, it would be not possible to analyze air mass transformation~~
93 ~~climatologically on the energy budgets along the trajectories of winter WaMAIs in any other way than relying on~~
94 ~~reanalysis. Here, we alleviate uncertainty in two ways: first, by averaging over a large number of cases and second,~~
95 ~~by considering anomalies rather than actual mean values. Avoiding single case studies reduces random errors,~~
96 ~~while considering anomalies reduces systematic errors.~~

97 2.2. WaMAI Detection

98 We identify WaMAIs by analyzing the vertically integrated northward moisture flux, f_w , over the ocean sectors
99 of Barents, Kara, Laptev, East Siberian, Chukchi and Beaufort Seas (Figure 1) separately. Among these sectors,
100 winter SIC only varies substantially over the years in the Barents and Kara Seas. North of $80^\circ N$ in the Barents
101 Sea, SIC has a statistically significant correlation with f_w (Figure 2a); locations that pass a $p < 0.05$ Student's t
102 test (stippled in Figure 2a) are considered the sensitive region. For the remaining sectors, all sea ice covered
103 locations are considered sensitive regions since they do not display winter trends in SIC. The mean f_w over the
104 sensitive regions, $\overline{f_w}$, is approximately normally distributed (Figure 2b and d), we define a WaMAIs as when $\overline{f_w} >$
105 0 (red lines in Figure 2c and e) and their maxima larger than the 95 percentile, while portions of WaMAIs when
106 $\overline{f_w}$ is larger than the 95-percentile are considered extreme moist intrusions (EMIs; blue lines in Figure 2c and e).

107 ~~Utilizing ERA5 reanalysis introduces uncertainty, especially for anything that comes from parameterized~~
108 ~~model physics such as cloud parameters and the energy budget. Large upward residual heat flux biases exist~~
109 ~~among all reanalysis and turbulent heat flux over the sea ice are also poorly simulated in all seasons (Graham et~~
110 ~~al., 2019). In the data assimilation, the main variables in a reanalysis are constrained by observations and in-situ~~
111 ~~observations over the central Arctic Ocean are sparse, especially in winter. The loss of all visible wavelengths in~~
112 ~~passive remote sensing in winter also makes many satellite products less trustworthy. However ERA-Interim, the~~
113 ~~predecessor of ERA5, generally performs best among the available reanalysis datasets, especially for the wind~~
114 ~~(Lindsay et al., 2014) and substantial progress has been made in data quality and diagnostic techniques during~~

115 last few decades (Mayer et al., 2019). However, it would be not possible to analyze air mass transformation
116 climatologically on the energy-budgets along the trajectories of winter WaMAIs in any other way than relying on
117 reanalysis. Here, we alleviate uncertainty in two ways: first, by averaging over a large number of cases and second,
118 by considering anomalies rather than actual mean values. Avoiding single case studies reduces random errors,
119 while considering anomalies reduces systematic errors.

120 **2.2. WaMAI Detection**

121 Clouds and moisture are integral and important parts of the Arctic surface and boundary-layer energy budgets and
122 relative humidity in the Arctic boundary layer is almost always high (Andreas et al., 2002; Persson et al., 2002).
123 Although it is possible to have a warm and dry air mass intruding in the Arctic, it is quite unlikely to have an
124 intrusion that is moist and cold. We therefore identify WaMAIs by analyzing the vertically integrated northward
125 moisture flux, f_w , separately over the ocean sectors of Barents, Kara, Laptev, East Siberian, Chukchi and Beaufort
126 Seas (Figure 1). Among these sectors, winter SIC only varies substantially with the time over the Barents and
127 Kara Seas. North of $80^\circ N$ in the Barents Sea, SIC has a statistically significant correlation with f_w (Figure 2a).
128 locations that pass a $p < 0.05$ Student's t-test (stippled in Figure 2a) are considered the sensitive region. For the
129 remaining sectors, all sea ice covered locations are considered sensitive regions since they do not display winter
130 variability in SIC. The mean f_w over each sensitive region, \bar{f}_w , are approximately normally distributed (Figure 2b
131 and d). We define a WaMAI as a continuous period when $\bar{f}_w > 0$ (red lines in Figure 2c and e) with a maximum
132 larger than the 95-percentile of the distribution of all values of \bar{f}_w . The portion of a WaMAIs when \bar{f}_w is larger
133 than the 95-percentile are moreover considered extreme moist intrusions (EMIs; blue line in Figure 2c and e);
134 note that each WaMAI can only include one EMI. The onset and terminal time of a WaMAI is taken at the nearest
135 minimum values of \bar{f}_w , or zero of \bar{f}_w .

136 Similar as You et al.(2021, 2020), ensembles of two day forward and backward trajectories at different
137 altitudes are calculated for each WaMAI over all ocean basins, using the trajectory algorithm from Woods et al.
138 (2013). The Over each ocean sectors and for each WaMAI, we select a launch points are takenpoint along a
139 latitude circle where the T850 at $75^\circ N$ is the largest. The latitude circle of $75^\circ N$ (blue lines in figure 2a; ~~$80^\circ N$~~)
140 is used for all ocean sectors, except for the Barents Sea, where $80^\circ N$ (red line in figure 2a) and forward is used.
141 Forward (backward) trajectories are also terminated where they start to track southward (northward). Hence, we
142 only capture the part of each trajectory that continuously tracks northwards. Finally, the terminal points of selected
143 trajectories have to be at least 5° north of the sea-ice edge, defined as where SIC exceeds 15%. Trajectories are
144 calculated at several different heights, every 100 m, from 300 m to 800 m and vertical profiles of the various
145 variables are then extracted from ERA5, from the surface to 2 km, by interpolation in time and space along each
146 of these trajectories. The final vertical cross-section for each WaMAI is the ensemble average of the results along
147 all trajectories for that WaMAI initialised at different heights. For the 40 winters in this study, 87 (131) WaMAIs
148 are detected over the ocean sectors with open ocean (land-locked sea ice) for a total of 218 WaMAIs.

149 **2.3. Energy Budgets**

150 As shown in Eq. 1, total surface energy-budget (F_{total}) is contributed by surface net solar irradiance (F_{sw}), surface
151 net thermal irradiance (F_{lw}), surface turbulent sensible heat fluxes (F_{sh}) and surface turbulent latent heat fluxes

Formatted: Font: Not Italic

Formatted: Font: Not Italic, Not Superscript/ Subscript

Formatted: Font: 11 pt

Formatted: Font: 11 pt

152 (F_{lh}). Note that all surface net energy fluxes contributing to a surface warming are considered positive. Individual
 153 terms in Eq. 1 are also interpolated from ERA5 at each 0.5-degree interval in latitude along the trajectories.

$$154 \quad F_{total} = F_{sw} + F_{lw} + F_{sh} + F_{lh} \quad (1)$$

155 We also evaluate the cloud longwave radiative effects (CRE) ($F_{lw_CRE} = F_{lw_all_sky} - F_{lw_clear_sky}$), using the
 156 same method. $F_{lw_all_sky}$ is the surface net thermal irradiance, considering the actual clouds presence, while
 157 $F_{lw_clear_sky}$ is clear-sky counterpart, assuming clouds were not present.

158 For the atmospheric energy budget calculations, we also extract the temperature tendencies due to different model
 159 physics from ERA5, where we can resolve all terms in the thermal equation (Eq. 2). As shown in Eq. 2, the total
 160 temperature tendency T_t of an air-mass in a WaMAI is contributed by heating/cooling from the divergence of
 161 shortwave irradiance ($\frac{\partial T}{\partial t_{sw}}$), longwave irradiance ($\frac{\partial T}{\partial t_{lw}}$) and vertical turbulent heat flux ($\frac{\partial T}{\partial t_{TH}}$) and the latent heat
 162 of condensation in cloud formation ($\frac{\partial T}{\partial t_{LH}}$). In a Lagrangian view, the advection tendencies are by definition zero,
 163 while in [Eulerian](#) view, the total tendencies would additionally be balanced by temperature advection. All
 164 these terms are also interpolated along the trajectories as previously discussed (also see You et al. 2020, 2021).

$$165 \quad T_t = \frac{\partial T}{\partial t_{sw}} + \frac{\partial T}{\partial t_{lw}} + \frac{\partial T}{\partial t_{LH}} + \frac{\partial T}{\partial t_{TH}} \quad (2)$$

166 Note that while the surface energy budget depends on the surface fluxes, the atmospheric energy budget depends
 167 [on](#) the vertical gradient of fluxes.

168

169

170 **3. Results**

171 **3.1 Large-scale Features**

172 EMIs were identified in the Arctic ocean basins of Barents, Kara, Laptev, East Siberian, Chukchi and Beaufort.
 173 Figure 3 (4) shows the composite of all EMIs over the Barents (Beaufort) Sea, representing the large-scale features
 174 of winter EMIs over ocean sectors with open ocean (land-locked sea ice). Both figure 3a and 4a show one pair of
 175 negative and positive GH_{500} anomalies with a large geopotential height gradient in between, generating an
 176 intensive f_w anomaly directed into the Arctic (Figure 3c, 4c), enhancing temperature advection (Figure 3b, 4b) and
 177 cloud formation (Figure 3d, 4d), consistent with previous studies (Tjernström et al. 2015; Overland and Wang
 178 2016; Gong and Luo 2017; Johansson et al., 2017; Sedlar and Tjernström 2017; Messori et al. 2018; Cox et al.
 179 2019; You et al., 2021). Unlike over the Barents Sea, where the TWP anomaly is dominated by LWP (Figure 4d
 180 and 4e), TWP over the Beaufort Sea is dominated by IWP. These features in the GH_{500} , T_{850} and TWP anomalies
 181 are also found in all other ocean basins- ([Figure S1, S3, S5](#)).

182 As warm and moist air is advected into the Arctic over the Barents Sea, it interacts with the cool ice
 183 surface through turbulence and radiation, enforcing positive F_{sh} , F_{lh} and F_{lw} anomalies at the surface (Figure 5c,
 184 5d and 5e). The F_{sh} anomaly reaches $> 60 \text{ W m}^{-2}$ over open water near the Norwegian coast, tapering off northward
 185 over the ice all the way to the pole. The pattern of F_{lh} anomaly is similar to that of F_{sh} south of 80°N , but decreases

186 to nearly zero over the sea ice north of 80°N. Positive LWP and IWP anomalies in figure 3d and 3e, extending
187 from the coast to the north pole along the path of the EMIs, also affects the surface energy-budget with a positive
188 F_{lw} anomaly (Figure 5c). This relation between F_{lw} anomaly and winter EMIs over the Barents Sea is also
189 discussed in other climatological analyses (Gong et al., 2017; Gong and Luo, 2017). In total, these anomalies in
190 the surface-energy fluxes sum up to a positive F_{total} anomaly, inducing decreased SIC (Figure 5b).

191 Similar surface energy-budget pattern is also found over the Beaufort Sea (Figure 6) **and other ocean**
192 **sectors with land-locked sea ice (Figure S2, S4, S6)**, but with some differences. The anomaly in F_{total} over the
193 Barents Sea is dominated by F_{sh} , while F_{total} anomaly over the Beaufort Sea is dominated by F_{lw} . The magnitudes
194 of F_{sh} , F_{lh} and F_{total} anomalies over the Beaufort Sea are less half the magnitude of those over the Barents Sea,
195 especially south of 80°N and hence induce four times less SIC decrease. As EMIs occur over the Beaufort Sea,
196 positive F_{sh} , F_{lh} , F_{total} , F_{lw} , LWP and IWP anomalies and negative SIC anomaly is found. However, negative F_{sh} ,
197 F_{lh} , F_{total} , F_{lw} , LWP and IWP anomalies and positive SIC anomalies could also be found over the Barents Sea
198 sector, while some WaMAIs from the Beaufort Sea pass through the pole and become cold spells over the Barents
199 Sea (Figure 4 and 6).

200 Table 1 summarizes the averaged surface energy-budgets over sea ice across the six basins. Except for
201 the Barents Sea, F_{lw} anomalies are almost twice larger than F_{sh} anomalies. Since F_{sw} anomalies can be ignored
202 in winter, the F_{lw} anomalies dominate F_{total} . However, over the Barents Sea, F_{sh} anomalies are almost twice larger
203 than F_{lw} anomalies and **contributes/contribute** to more than 50% of F_{total} anomalies. Over the Barents and Chukchi
204 Sea, positive F_{sh} anomalies are statistically significant, which is not the case for any of the other sectors. Except
205 for the Laptev Sea, positive F_{total} and F_{lw} anomalies are statistically significant.

206 The composites of large-scale pattern discussed above are extracted from the stronger EMI events to
207 generate a clear signal, however, these may not necessarily represent the general pattern of all WaMAIs. Therefore,
208 linear regressions of daily averaged GH, T_{850} , SIC, F_{total} , F_{sh} , F_{lh} , F_{sw} and F_{lw} anomaly against the time series of
209 daily averaged \bar{f}_w over the sensitive regions in recent 40 winters were calculated separately for all the examined
210 ocean basins. All the regressed fields have similar pattern as their counterparts in Figures 3~6, implying a similar
211 relationship for all **WaMAIs/days** but at smaller magnitudes. Since the regressions confirm the conclusions, we
212 will consider only the Barents and Beaufort Seas as an example of ocean sector with open ocean and land-locked
213 sea ice, respectively (Figure 7 and 8).

214

215 3.2 The Surface Energy-budget

216 In this section, we will explore the transformation of temperature inversion, cloud formation and surface energy-
217 budget along the trajectories of warm-and-moist air masses over ocean basins with open water and land-locked
218 sea ice, respectively, by **composite/compositing** the heights to the maximum specific humidity (h_{sh}), temperature
219 (h_t) and vertical temperature gradient (h_{tz}), along with TWP, LWP, IWP, precipitation rate (PRCR) and surface
220 energy-budget terms (F_{sh} , F_{lh} , F_{total} , F_{lw}) from all detected WaMAIs.

221 Over the completely ice-covered sea sectors such as the Laptev, East Siberia, Chukchi and Beaufort Seas, strong
222 temperature inversion develops with cloud formation below, as the warm-and-moist air propagates over the sea

223 ice. ~~A detailed analysis of this boundary layer structure follows in Section 3.3.~~ In this case, h_{sh} is ~~above~~ higher
224 ~~than~~ h_t , and both ~~are~~ higher than h_{tz} (Figure 9a). From the ice edge and onward up to 10 degrees north of the ice
225 edge, h_{sh} , h_t and h_{tz} increase almost linearly, by 30–40 m ~~per degree~~ $^{\circ}$ latitude (Figure 9a) ~~as the inversion is~~
226 ~~lifted~~. TCW and PRCP also increase northward, although more slowly for the first two degrees, in total by 6 g m^{-2}
227 ~~degree~~ $^{-1}$ and 0.4 mm day^{-1} ~~per degree~~ $^{\circ}$ latitude, respectively, implying that stratocumulus develop continuously
228 along the trajectories (Figure 9b, c). The increasing TWP is mainly due to the increase in IWP since LWP is
229 almost constant along the trajectories (Figure 9b). The increase of h_{tz} is comparable to that of summer WaMAIs,
230 while the increase in TWP is about half of that of summer WaMAIs (You et al., 2021), since less moisture is
231 available for cloud development in winter (Figure 4c).

232 The gradual increase of h_{tz} , a manifestation of increased boundary-layer mixing, leads to a reduction in ~~near-~~
233 near-surface gradients. Since the turbulent heat fluxes at the surface ~~are dependent~~ depend on these gradients, ~~the~~
234 F_{sh} anomaly decreases gradually at a rate of 1.5 W m^{-2} ~~per degree~~ $^{\circ}$ latitude (Figure 10a). Simultaneously, ~~the~~ F_{lw}
235 anomaly increases almost linearly by 2.5 W m^{-2} ~~per degree~~ $^{\circ}$ latitude, while F_{th} , the smallest contributor to F_{total} ,
236 ~~are~~ is almost constant along the trajectories (Figure 10a). The increase in F_{lw} along trajectories is due to ~~the increase~~
237 ~~in the~~ increasing cloud radiative effects ~~of~~ by the ~~evolving~~ stratocumulus. ~~As shown in figure 10b, clouds;~~
238 F_{lw_CRE} increases at a similar rate as F_{lw} (Figure 10b). From 0 to 2 degrees north of the sea ice edge, ~~the~~ F_{total}
239 anomaly is dominated by ~~the~~ F_{sh} anomaly, while farther north it is dominated by F_{lw} anomaly (Figure 10a).
240 Generally, F_{total} anomaly increases with the distance from the sea ice edge at a rate of 1 W m^{-2} ~~(degree~~ $^{\circ}$ latitude) $^{-1}$
241 and this increasing trend is dominated by F_{lw} anomaly (Figure 10a).

242 Over the Barents Sea, with open warm water south of the ice edge, h_t and h_{sh} also increase nearly linearly
243 but at a ~~rate~~ 1.6 times larger rate than ~~for those over~~ ocean sectors with land-locked sea ice, however, ~~starting~~ at
244 considerably smaller values (Figure 9d). The ~~maximum values of h_t and h_{sp} here are comparable to the~~ minimum
245 values ~~of h_t and h_{sp} over these~~ ~~the~~ completely ice-covered sectors ~~are comparable to the maximum values over the~~
246 ~~Barents Sea~~, implying that WaMAIs over the Barents Sea ~~develops a shallower well-mixed layer and hence~~ bring
247 the moist and warm air closer to the surface ~~with a shallower PBL~~. However, the temperature inversion over the
248 Barents Sea is too weak to be easily identified with the metrics used above. Unlike for the sectors with land-locked
249 sea ice, TWP and PRCP are constant with downwind distance from the ice edge, varying slightly around 150 g
250 m^{-2} and 7 mm day^{-1} (Figure 9e, f). As a consequence, F_{lw} anomaly and F_{lw_CRE} along the trajectories (Figure 10c,
251 d) are nearly constant with northward distance. Although TWP remains quasi-constant, LWP (IWP) decreases
252 (increases) at a rate of -6 g m^{-2} ($+6 \text{ g m}^{-2}$) along the trajectories (Figure 9e). From 0 to 4 degrees north of the sea
253 ice edge, TWP is contributed by LWP and IWP in about equal parts, while from 4 degrees north of the sea ice
254 edge and onward, TWP gradually becomes dominated by IWP.

255 ~~The~~ F_{sh} anomaly decreases fast by nearly 50% over the first two degrees from the sea ice edge (Figure
256 10c). From 2 to 10 degrees north of the sea ice edge, the decrease is more moderate at a rate of 4 W m^{-2} ~~per degree~~
257 $^{\circ}$ latitude (Figure 10c) ~~but~~, ~~which is~~ still faster than that over the completely frozen ocean sectors. However, ~~the~~
258 F_{sh} anomaly ~~even at ten degrees north of the ice edge~~ is still larger than the largest ~~corresponding~~ value ~~of F_{sh}~~
259 ~~anomaly over~~ the completely frozen ocean sectors ~~, even ten degrees north of the ice edge~~ (Figure 10a). This
260 is likely due to the much warmer upstream conditions over the open ocean. The large thermal contrast between
261 open ocean and sea ice surface contributes to the stable atmospheric layer over the sea ice surface and rapidly

Formatted: Indent: First line: 1.11 cm, Tab stops: 4.92 cm, Left

262 reducing F_{sh} anomaly, while the decrease of F_{sh} anomaly with downstream distance is due to the slowly reducing
263 temperature gradient ~~resulted~~resulting from the turbulent mixing. Similar decreasing trends are also present for
264 F_{lh} and F_{total} anomaly (Figure 10c). From 2 to 10 degrees north of the sea ice edge, they decrease at a rate of 1 and
265 5 W m^{-2} ~~per degree~~+ latitude, respectively (Figure 10c). Within 5 degrees north of the sea ice edge, F_{total} anomaly
266 is dominated by F_{sh} , while downstream the turbulent heat flux ($F_{sh} + F_{lh}$) anomaly becomes comparable to F_{lw}
267 anomaly and contribute almost equally to F_{total} anomaly (Figure 10c).

268 Without the presence of solar radiation in winter, the variation of F_{total} anomaly over the Barents Sea is
269 dominated by F_{sh} anomaly (Figure 10a), while it is dominated by F_{lw} anomaly over ocean sectors with land-locked
270 sea ice (Figure 10c). This distinction between ocean sectors with and without open ocean upstream can be
271 explained by the stronger air-sea interaction over the Barents Sea (Kim et al., 2019). Before the air-mass is
272 advected in over the sea ice, it is heated and moistened by the ~~warmer and moister~~ocean ~~surface~~ and consequently,
273 exerts greater turbulent heat fluxes to the surface as it suddenly enters over the sea ice (Figure 10c). ~~Also, the~~
274 ~~cloud~~Cloud formation happens already upstream over the warm water and ~~is in a much deeper PBL and is hence~~
275 not much affected by the advection over sea ice. ~~Instead a much shallower well-mixed layer forms as the air enters~~
276 ~~over the ice, and the larger vertical gradients resulting from the large temperature difference across the ice edge~~
277 ~~gives rise to larger F_{sh} .~~ This dominance of turbulent heat fluxes remains until the halfway along the trajectories.

278 3.3 The Boundary-layer Energy-budget

279 As discussed in previous sections, cloud formation as part of the air-mass transmission can exert large variability
280 on the surface energy-budget. Here, we focus on the cloud effects on the boundary-layer energy-budget. For each
281 WaMAI, the boundary-layer energy-budget terms are evaluated and interpolated along the trajectory and analyzed
282 on a case-by-case basis, categorizing patterns into four main categories: a) lifting temperature inversion (INV); b)
283 radiation-dominated (RAD); c) turbulence-dominated (TBL); and d) turbulence-dominated with cold dome (TCD).
284 Some typical cases are shown in figure 11-14 ~~respectively for these four categories~~, illustrating different
285 boundary-layer energy-budgets in each category, ~~while conceptual summary graphs of all the different categories~~
286 ~~are summarized in Figure 15.~~

287 ~~All ocean sectors fall within either of these, except for the Kara Sea that has some sea ice variability and~~
288 ~~open ocean. Hence, some WaMAIs behave as typical for the Barents Sea, while most behave like for the other~~
289 ~~sectors with land-locked sea ice.~~ Almost all WaMAIs over ocean sectors with land-locked sea ice feature a
290 boundary-layer energy-budget pattern of category INV. Similar to category TBL for summer WaMAIs (You et
291 al., 2021), category INV is characterized by increasingly lifting temperature inversion and continuously
292 stratocumulus development near the inversion. Different from the ocean sectors with land-locked sea ice, clouds
293 during WaMAIs over the ocean sector with ~~an~~ upstream open ocean (e.g. Barents Sea) form at the altitude of ~1
294 km, above the warm-and-moist air-masses. The boundary-layer energy-budget here is categorized into three
295 categories (RAD, TBL, TCD). Category RAD is characterized by stronger cloud-top radiative cooling and related
296 buoyant mixing, while category TBL is characterized by more intensive surface turbulent mixing. Category TCD
297 is similar to category TBL excluding a cold dome over the high Arctic. ~~The boundary-layer energy-budget patterns~~
298 ~~are categorized by manually checking case by case if they have the typical characteristics of each categories. Their~~
299 ~~launch time and launch longitudes are listed in table S1.~~

300 Note that unlike radiation and condensation/evaporation, turbulence does not generate heating/cooling
 301 by itself. Instead, it heats/cools air locally by redistributing heat from one altitude to another through mixing
 302 within the column. Also, note that the temperature tendencies discussed below are only those that are due to model
 303 physics in a Lagrangian view, while in an Eulerian framework, they would be balanced by advection (not shown).
 304 In an absolute sense the boundary layer always undergoes a gradual cooling during the advection over the sea ice.
 305 *Conceptual graphs of all the different categories are summarized in Figure 15.*

3.3.1 Lifting temperature inversion (INV)

307 *In this category turbulent heating and cooling dominate the boundary-layer energy-budget (Figure 11e and 11h),
 308 even though stratocumulus develops along the trajectories and affects the radiative processes (Figure 11a and f).
 309 Turbulent mixing transports heat from the upper to the lower parts of the PBL, hence cooling the upper and
 310 warming the lower parts of the PBL (Figure 11h). Since the turbulent mixing persists along the trajectories, the
 311 well-mixed layer below the inversion continuously deepens northward (Figure 11b), while the inversion and the
 312 cloud-top are gradually lifted (Figure 11a). This supports the hypothesis from Tjernström et al. (2019b), that the
 313 surface inversion formed at the sea-ice edge is eroded progressively downstream, by cloud-top cooling and surface
 314 turbulent mixing, and eventually the boundary layer must transform into the often observed well-mixed cloud-
 315 capped boundary layer (Morrison et al., 2012; Pithan et al., 2014; Sotiropoulou et al., 2014; Tjernström et al.,
 316 2012; Tjernström and Graversen, 2009). Even though this hypothesis was originally posed for summer WaMAIs,
 317 it is also applicable for winter WaMAIs over completely frozen ocean sectors; see Figure 15a.*

3.3.1 Lifting temperature inversion (INV)

319 *In this category turbulent heating and cooling dominate the boundary-layer energy-budget (Figure 11e and 11h),
 320 even though stratocumulus develops along the trajectories and affects the radiative processes (Figure 11a and f).
 321 Turbulent mixing transports heat from the upper to the lower parts of the PBL, hence cooling the upper and
 322 warming the lower parts of the PBL (Figure 11h). Since the turbulent mixing persists along the trajectories, the
 323 well-mixed layer below the inversion continuously deepens northward (Figure 11b), while the inversion and the
 324 cloud top are gradually lifted (Figure 11a). This supports the hypothesis from Tjernström et al. (2019), that the
 325 surface inversion formed at the sea ice edge is eroded progressively downstream, by cloud-top cooling and surface
 326 turbulent mixing, and eventually the boundary layer must transform into the often observed well-mixed cloud-
 327 capped boundary layer (Brooks et al., 2017; Graversen et al., 2008; Morrison et al., 2012; Pithan et al., 2014;
 328 Sotiropoulou et al., 2014; Tjernström et al., 2012; Tjernström and Graversen, 2009). Even though this hypothesis
 329 was originally posed for summer WaMAIs, it is also applicable to winter WaMAIs over completely frozen ocean
 330 sectors; see Figure 15a.*

331 Clouds are relatively thin and radiative cooling near the cloud top is therefore weak (Figure 11f) and
 332 only in a few cases the magnitude of radiative cooling is comparable to the turbulent cooling. Generally, in this
 333 category, turbulent heating is larger than radiative heating as well as latent heating, and hence boundary-layer
 334 warming is dominated by turbulence, but since turbulence only redistribute heat inside the PBL, as a whole it is
 335 gradually cooled as the warm air progresses northward.

3.3.2 Radiation-dominated (RAD)

337 Over the Barents Sea, the maximum air temperature (Figure 12a, 13a, 14a) and specific humidity (Figure 12d,
338 13d, 14d) over open ocean south of the ice edge are always located right above the sea surface as a result of the
339 strong air-sea interaction and are also typically larger than those over ocean sectors with land-locked sea ice. As
340 this air-mass, considerably affected by air-sea interaction, is advected over the sea ice, different stories take place.

341 Around 8% of all WaMAIs over the Barents Sea belong to category RAD (Table 2). In this category, the
342 total temperature tendencies are forced by radiative processes. For this category, the large-scale subsidence is an
343 order of magnitude smaller than that in category TBL (Table 3, CONV) and LWP is three times larger than that
344 in category TCD (Table 3, LWP), suggesting that the stratocumulus develops more intensively in category RAD
345 (Figure 12a). With larger values of LWP, longwave radiation is effectively emitted at the cloud top like a black
346 body, exerting large cooling rates with maximum reaching -16 K day^{-1} . However, unlike the cloud formation in
347 category INV, here clouds always already form south of the ice edge over the open water and few clouds develop
348 in the near-surface inversion. In the cloud, heat is redistributed with warming at the cloud top and cooling in the
349 lower PBL by buoyant mixing driven by cloud-top longwave radiative cooling (Figure 12h). The turbulent cooling
350 layer in the PBL interior is apparently thicker than the turbulent warming layer whose absolute value of heating
351 rate is considerably more intensive (Figure 12h). As shown in figure 12h, the buoyant mixing can access the surface
352 and induce a thicker well-mixed layer below the stratocumulus (Figure 12b). As precipitation constantly erodes
353 the cloud, buoyant mixing continuously provides moisture for the cloud development from the moister air below
354 and hence cloud development as well as the cloud top cooling is maintained.

355 Meanwhile, the value of maximum temperature and specific humidity is decreasing gradually along the
356 trajectory, indicating that the heat and moisture within the warm-and-moist air is consumed continuously by the
357 cloud formation and surface turbulent mixing. For this category, F_{tw} is comparable to those of category TBL and
358 TCD (Table 3), and increases almost linearly along the trajectory (Figure 16d1) due to the enhancing TWP (Figure
359 16c1). F_{sh} and F_{th} are generally smaller than those of category TBL since stronger mixing weakens vertical
360 gradients in the PBL and hence suppresses the surface turbulent heat flux (Table 3). The decreasing rates of F_{sh}
361 and F_{th} from 0 to 2 degrees north of the sea ice edge are larger than for categories TBL and TCD as a result of
362 stronger buoyant mixing in the PBL (Figure 16a1), while onwards, their decreasing rates are smaller than those
363 for the other two categories since the lifting rates of h_t and h_{sp} are dramatically slowed down (Figure 16b1); see
364 Figure 15b.

365 3.3.3 Turbulence-dominated (TBL)

366 52% of WaMAIs over the Barents Sea belong to the turbulence dominated category. The variation of surface
367 energy-budget along the trajectory (Figure 16 a2, b2 and c2) is similar to the mean variation of WaMAIs from all
368 categories showed in figure 10c and 10d. Subsidence for WaMAIs in this category is typically a factor of three
369 larger than that in category RAD and it is statistically significantly positive (Table 3, CONV). Consequently,
370 clouds in this category do not develop as intensively as in category RAD and hence the radiative cooling rate at
371 the cloud top is considerably smaller. The boundary-layer energy-budget is mainly dominated by turbulent heating
372 near the surface. As warm-and-moist air is advected into the Arctic sea ice, turbulence exchanges heat between
373 warm and cold air-mass by cooling (heating) warmer (colder) air (Figure 13h), simultaneously inducing a
374 gradually thickening well-mixed layer capped by a strong inversion, and a continuously lifting of h_t and h_{sp} (Figure

375 13b). In this category, the well-mixed layer is substantially thinner than in category RAD, since the turbulent
376 mixing here is mainly forced by surface friction, weaker and less effective than the buoyant mixing in category
377 RAD (Figure 12b). Turbulence is mainly forced by wind shear and buoyancy, but buoyancy is negative here in
378 the initially very stable near-surface layer. Therefore, wind shear mostly fuels the turbulent mixing. In category
379 TBL, turbulent mixing is stronger than in category RAD, but the surface fluxes are still stronger, due to the
380 stronger gradients; F_{sh} and F_{lh} are 77% and 42% larger than those in category RAD. Also see Figure 15c.

381 3.3.4 Turbulence-dominated with cold dome (TCD)

382 40% of WaMAIs over the Barents Sea belong to this category. For this category, the boundary-layer energy-
383 budget is generally similar to that in category TBL. The main difference is that there is always a layer of cold air
384 (cold dome) laying below the warm-and-moist air-mass especially in the central Arctic (Figure 14c). This cold
385 dome enlarges the vertical temperature gradient and hence intensifies turbulent heat near the surface (Figure 14h).
386 As the warm-and-moist air-mass is advected over the cold dome, it is gradually lifted up by the cold dome and
387 consequently, h_t and h_{sp} are increasing at a faster rate than in category TBL (Figure 16b3). With faster lifting h_t
388 and h_{sp} , F_{sh} and F_{lh} would be reduced more rapidly or even become negative in the high Arctic (Figure 16a3).
389 ~~Unlike in category RAD, where~~ TWP is dominated by LWP; ~~in category RAD and category TBL, where~~ TWP is
390 contributed almost equally by LWP and IWP; ~~in this category TBL, while in~~ category TCD, TWP is gradually
391 more dominated by IWP; the IWP-to-TWP ratio increases linearly from ~50% to ~100% (Figure 16c3); also see
392 Figure 15d.

393 4. Conclusion

394 Warm-and-moist air intrusions (WaMAI) greatly contribute to Arctic surface warming. To understand the surface
395 and boundary-layer energy-budget as WaMAIs occur, in this paper, we have detected WaMAIs over the Arctic
396 Ocean sectors of Barents, Kara, Laptev, East Siberian, Chukchi and Beaufort Seas in 40 recent winters (DJF from
397 1979 to 2018) using ERA5 reanalysis. The climatological analysis shows a consistent pattern with a blocking
398 high-pressure system over corresponding ocean sectors contribute to warm-and-moist air intrusions into winter
399 Arctic, supplying moisture for cloud formation, exerting a positive total energy-budget anomaly on the surface.

400 Statistically, as warm-and-moist air is advected over ocean sectors with land-locked ice cover, such as
401 the Laptev, East Siberian, Chukchi and Beaufort Seas, the longwave irradiance anomaly increases linearly by 2.5
402 $\text{W m}^{-2} (\text{degree}^{-1} \text{latitude})^{-1}$, while the total column cloud liquid water increases linearly by 6 $\text{g m}^{-2} (\text{degree}^{-1} \text{latitude})$
403 ⁻¹. ~~The longwave irradiance is dominant in the surface energy-budget.~~ We have also analysed the boundary-layer
404 vertical structure along these trajectories, as well as the associated surface energy-budget pattern of over these
405 sectors, and find one main category, elevated lifting temperature inversion (INV), which in structure is similar to
406 summer WaMAIs (You et al., 2021) (Figure 15a).

407 ~~During~~ WaMAIs over the Barents Sea, ~~with where~~ open ~~ocean-water exists to the~~ south of the ~~sea ice~~
408 edge, ~~are found in three~~ ~~turbulent heat flux is dominant over the surface energy-budget, especially along the first~~
409 ~~half-way of the trajectories~~ (Figure 10c). This difference on the surface energy-budget between the Barents Sea
410 ~~and frozen sea sectors is also preliminarily discussed by Lee et al. (2017). Three main categories: are found:~~
411 radiation-dominated (category RAD), turbulence-dominated (category TBL) and turbulence-dominated with cold

412 dome (category TCD), comprising 8%, 52% and 40%, respectively, of all WaMAIs. Unlike over the sectors with
413 land-locked sea ice, air-masses over the ice-free Barents Sea ~~is~~are warmed by the sea surface (local process) before
414 ~~being~~ advected over the sea ice (remote process), consequently resulting in more intensive surface warming.

415 In response to ten times smaller large-scale subsidence, stratocumulus develops more strongly in
416 category RAD with more intensive cloud-top radiative cooling, inducing apparently thicker well-mixed layer
417 (Figure 15b). However, this strong radiative cooling induces intensive buoyant mixing extending from the cloud
418 top till the surface, suppresses the surface turbulent mixing and decreases the lifting rate of the height to the
419 maximum temperature (h_t) and to the maximum specific humidity (h_{sp}). Therefore, surface turbulent fluxes in
420 category RAD and the lifting rate of h_t and h_{sp} are apparently smaller than those in category TBL (Figure 15c).
421 With cold dome, less liquid cloud water could be formed and fewer or even negative turbulent fluxes could access
422 to the surface, in comparison with category TBL (Figure 15d). In category TCD, turbulent fluxes decrease faster
423 along the trajectory since warm-and-moist air is lifted to higher altitude above the cold dome (Figure 15d).

424 Under the background of global warming, the rate of local process has been accelerated by 9% per year
425 (Kim et al., 2019), while the meridional heat and moisture transports (remote processes) over the Barents Sea are
426 also enhanced in recent decades (Nygård et al., 2020). This implies that WaMAI may play a more significant role
427 in the future Arctic warming. Therefore, the potential mechanism which enhances the occurrence and intensity of
428 WaMAI deserves more attentions from atmospheric scientists.

429 **Data availability**

430 All data used can be found on the ERA5 data repository at DOI: [www.ecmwf.int/en/forecasts/datasets/reanalysis-](https://www.ecmwf.int/en/forecasts/datasets/reanalysis-datasets/era5)
431 [datasets/era5](https://www.ecmwf.int/en/forecasts/datasets/reanalysis-datasets/era5).

432 **Author contributions**

433 CY conducted analysis and interpretation of the data under the supervision of MT and AD. CY prepared the
434 original version of the paper. MT and AD provided constructive comments and revisions to the final article.

435 **Competing interests**

436 The authors declare that they have no conflict of interest.

437 **Acknowledgements:**

438 This research was supported by the Swedish Research Council under Grant 2016-03807. The authors are grateful
439 to Cian Woods for providing the trajectory calculation algorithm.

440

441

442 **References**

- 443
- 444 [Ali, S. M. and Pithan, F.: Following moist intrusions into the Arctic using SHEBA observations in a Lagrangian](#)
- 445 [perspective, Q. J. R. Meteorol. Soc., 146\(732\), 3522–3533, doi:10.1002/qj.3859, 2020.](#)
- 446 [Andreas, E. L., Guest, P. S., Persson, P. O. G., Fairall, C. W., Horst, T. W., Moritz, R. E. and Semmer, S. R.:](#)
- 447 [Near-surface water vapor over polar sea ice is always near ice saturation, J. Geophys. Res. Ocean.,](#)
- 448 [doi:10.1029/2000jc000411, 2002.](#)
- 449 [Brooks, I. M., Tjernström, M., Persson, P. O. G., Shupe, M. D., Atkinson, R. A., Canut, G., Birch, C. E.,](#)
- 450 [Mauritsen, T., Sedlar, J. and Brooks, B. J.: The Turbulent Structure of the Arctic Summer Boundary Layer](#)
- 451 [During The Arctic Summer Cloud-Ocean Study, J. Geophys. Res. Atmos., 122\(18\), 9685–9704,](#)
- 452 [doi:10.1002/2017JD027234, 2017.](#)
- 453 Cohen, J., Screen, J. A., Furtado, J. C., Barlow, M., Whittleston, D., Coumou, D., Francis, J., Dethloff, K.,
- 454 Entekhabi, D., Overland, J. and Jones, J.: Recent Arctic amplification and extreme mid-latitude weather, Nat.
- 455 Geosci., 7(9), 627–637, doi:10.1038/ngeo2234, 2014.
- 456 Cox, C. J., Stone, R. S., Douglas, D. C., Stanitski, D. M. and Gallagher, M. R.: The Aleutian Low-Beaufort Sea
- 457 Anticyclone: A Climate Index Correlated With the Timing of Springtime Melt in the Pacific Arctic Cryosphere,
- 458 Geophys. Res. Lett., 46(13), 7464–7473, doi:10.1029/2019GL083306, 2019.
- 459 [Francis, J. A. and Vavrus, S. J.: Evidence linking Arctic amplification to extreme weather in mid-latitudes,](#)
- 460 [Geophys. Res. Lett., 39\(6\), doi:10.1029/2012GL051000, 2012.](#)
- 461 Gong, T. and Luo, D.: Ural blocking as an amplifier of the Arctic sea ice decline in winter, J. Clim., 30(7),
- 462 2639–2654, doi:10.1175/JCLI-D-16-0548.1, 2017.
- 463 Gong, T., Feldstein, S. and Lee, S.: The role of downward infrared radiation in the recent arctic winter warming
- 464 trend, J. Clim., 30(13), 4937–4949, doi:10.1175/JCLI-D-16-0180.1, 2017.
- 465 [Graham, R. M., Cohen, L., Ritzhaupt, N., Segger, B., Graverson, R. G., Rinke, A., Walden, V. P., Granskog, M.](#)
- 466 [A. and Hudson, S. R.: Evaluation of six atmospheric reanalyses over Arctic sea ice from winter to early summer,](#)
- 467 [J. Clim., 32\(14\), 4121–4143, doi:10.1175/JCLI-D-18-0643.1, 2019.](#)
- 468 Graverson, R. G., Mauritsen, T., Tjernström, M., Källén, E. and Svensson, G.: Vertical structure of recent Arctic
- 469 warming, Nature, 451(7174), 53–56, doi:10.1038/nature06502, 2008a.
- 470 Graverson, R. G., Mauritsen, T., Tjernström, M., Källén, E. and Svensson, G.: Vertical structure of recent Arctic
- 471 warming, Nature, 451(7174), 53–56, doi:10.1038/nature06502, 2008b.
- 472 Hersbach, H., Bell, B., Berrisford, P., Hirahara, S., Horányi, A., Muñoz-Sabater, J., Nicolas, J., Peubey, C.,
- 473 Radu, R., Schepers, D., Simmons, A., Soci, C., Abdalla, S., Abellan, X., Balsamo, G., Bechtold, P., Biavati, G.,
- 474 Bidlot, J., Bonavita, M., De Chiara, G., Dahlgren, P., Dee, D., Diamantakis, M., Dragani, R., Flemming, J.,
- 475 Forbes, R., Fuentes, M., Geer, A., Haimberger, L., Healy, S., Hogan, R. J., Hólm, E., Janisková, M., Keeley, S.,

476 Laloyaux, P., Lopez, P., Lupu, C., Radnoti, G., de Rosnay, P., Rozum, I., Vamborg, F., Villaume, S. and
477 Thépaut, J. N.: The ERA5 global reanalysis, *Q. J. R. Meteorol. Soc.*, 146(730), 1999–2049,
478 doi:10.1002/qj.3803, 2020.

479 Kim, B. M., Son, S. W., Min, S. K., Jeong, J. H., Kim, S. J., Zhang, X., Shim, T. and Yoon, J. H.: Weakening of
480 the stratospheric polar vortex by Arctic sea-ice loss, *Nat. Commun.*, doi:10.1038/ncomms5646, 2014.

481 Kim, K. Y. and Son, S. W.: Physical characteristics of Eurasian winter temperature variability, *Environ. Res.*
482 *Lett.*, doi:10.1088/1748-9326/11/4/044009, 2016.

483 Kim, K. Y., Kim, J. Y., Kim, J., Yeo, S., Na, H., Hamlington, B. D. and Leben, R. R.: Vertical Feedback
484 Mechanism of Winter Arctic Amplification and Sea Ice Loss, *Sci. Rep.*, doi:10.1038/s41598-018-38109-x,
485 2019.

486 Komatsu, K. K., Alexeev, V. A., Repina, I. A. and Tachibana, Y.: Poleward upgliding Siberian atmospheric
487 rivers over sea ice heat up Arctic upper air, *Sci. Rep.*, 8(1), doi:10.1038/s41598-018-21159-6, 2018.

488 [Lee, S., Gong, T., Feldstein, S. B., Screen, J. A. and Simmonds, I.: Revisiting the Cause of the 1989–2009](#)
489 [Arctic Surface Warming Using the Surface Energy Budget: Downward Infrared Radiation Dominates the](#)
490 [Surface Fluxes, *Geophys. Res. Lett.*, doi:10.1002/2017GL075375, 2017.](#)

491 [Li, M., Luo, D., Simmonds, I., Dai, A., Zhong, L. and Yao, Y.: Anchoring of atmospheric teleconnection](#)
492 [patterns by Arctic Sea ice loss and its link to winter cold anomalies in East Asia, *Int. J. Climatol.*,](#)
493 [doi:10.1002/joc.6637, 2021.](#)

494 [Lindsay, R., Wensnahan, M., Schweiger, A. and Zhang, J.: Evaluation of seven different atmospheric re analysis](#)
495 [products in the arctic, *J. Clim.*, 27\(7\), 2588–2606, doi:10.1175/JCLI-D-13-00014.1, 2014.](#)

496 Liu, Y., Key, J. R., Vavrus, S. and Woods, C.: Time evolution of the cloud response to moisture intrusions into
497 the Arctic during Winter, *J. Clim.*, 31(22), 9389–9405, doi:10.1175/JCLI-D-17-0896.1, 2018.

498 [Luo, B., Luo, D., Wu, L., Zhong, L. and Simmonds, I.: Atmospheric circulation patterns which promote winter](#)
499 [Arctic sea ice decline, *Environ. Res. Lett.*, doi:10.1088/1748-9326/aa69d0, 2017.](#)

500 [Luo, D., Chen, X., Overland, J., Simmonds, I., Wu, Y. and Zhang, P.: Weakened potential vorticity barrier](#)
501 [linked to recent winter Arctic Sea ice loss and midlatitude cold extremes, *J. Clim.*, doi:10.1175/JCLI-D-18-](#)
502 [0449.1, 2019.](#)

503 [Mayer, M., Tietsche, S., Haimberger, L., Tsubouchi, T., Mayer, J. and Zuo, H. A. O.: An improved estimate of](#)
504 [the coupled Arctic energy budget, *J. Clim.*, doi:10.1175/JCLI-D-19-0233.1, 2019.](#)

505 Messori, G., Woods, C. and Caballero, R.: On the drivers of wintertime temperature extremes in the high arctic,
506 *J. Clim.*, 31(4), 1597–1618, doi:10.1175/JCLI-D-17-0386.1, 2018.

507 Mori, M., Watanabe, M., Shiogama, H., Inoue, J. and Kimoto, M.: Robust Arctic sea-ice influence on the
508 frequent Eurasian cold winters in past decades, *Nat. Geosci.*, doi:10.1038/ngeo2277, 2014.

509 Morrison, H., De Boer, G., Feingold, G., Harrington, J., Shupe, M. D. and Sulia, K.: Resilience of persistent

510 Arctic mixed-phase clouds, *Nat. Geosci.*, 5(1), 11–17, doi:10.1038/ngeo1332, 2012.

511 Nygård, T., Naakka, T. and Vihma, T.: Horizontal moisture transport dominates the regional moistening patterns
512 in the arctic, *J. Clim.*, doi:10.1175/JCLI-D-19-0891.1, 2020.

513 Overland, J. E. and Wang, M.: Recent extreme arctic temperatures are due to a split polar vortex, *J. Clim.*,
514 29(15), 5609–5616, doi:10.1175/JCLI-D-16-0320.1, 2016.

515 Overland, J. E., Wood, K. R. and Wang, M.: Warm Arctic-cold continents: Climate impacts of the newly open
516 arctic sea, *Polar Res.*, doi:10.3402/polar.v30i0.15787, 2011.

517 [Papritz, L.: Arctic lower-tropospheric warm and cold extremes: Horizontal and vertical transport, diabatic
518 processes, and linkage to synoptic circulation features, *J. Clim.*, doi:10.1175/JCLI-D-19-0638.1, 2020.](#)

519 [Papritz, L., Hauswirth, D. and Hartmuth, K.: Moisture origin, transport pathways, and driving processes of
520 intense wintertime moisture transport into the Arctic, *Weather Clim. Dyn.*, 3\(1\), 1–20, doi:10.5194/wcd-3-1-
521 2022, 2022.](#)

522 [Persson, P. O. G., Fairall, C. W., Andreas, E. L., Guest, P. S. and Perovich, D. K.: Measurements near the
523 Atmospheric Surface Flux Group tower at SHEBA: Near-surface conditions and surface energy budget, *J.
524 Geophys. Res. Ocean.*, doi:10.1029/2000jc000705, 2002.](#)

525 Petoukhov, V. and Semenov, V. A.: A link between reduced Barents-Kara sea ice and cold winter extremes over
526 northern continents, *J. Geophys. Res. Atmos.*, doi:10.1029/2009JD013568, 2010.

527 Pithan, F., Medeiros, B. and Mauritsen, T.: Mixed-phase clouds cause climate model biases in Arctic wintertime
528 temperature inversions, *Clim. Dyn.*, 43(1–2), 289–303, doi:10.1007/s00382-013-1964-9, 2014.

529 [Pithan, F., Svensson, G., Caballero, R., Chechin, D., Cronin, T. W., Ekman, A. M. L., Neggers, R., Shupe, M.
530 D., Solomon, A., Tjernström, M. and Wendisch, M.: Role of air-mass transformations in exchange between the
531 Arctic and mid-latitudes, *Nat. Geosci.*, 11\(11\), 805–812, doi:10.1038/s41561-018-0234-1, 2018.](#)

532 [Rudeva, I. and Simmonds, I.: Midlatitude winter extreme temperature events and connections with anomalies in
533 the arctic and tropics, *J. Clim.*, doi:10.1175/JCLI-D-20-0371.1, 2021.](#)

534 [Screen, J. A. and Simmonds, I.: The central role of diminishing sea ice in recent Arctic temperature
535 amplification, *Nature*, doi:10.1038/nature09051, 2010.](#)

536 [Screen, J. A., Bracegirdle, T. J. and Simmonds, I.: Polar Climate Change as Manifest in Atmospheric
537 Circulation, *Curr. Clim. Chang. Reports*, doi:10.1007/s40641-018-0111-4, 2018.](#)

538 Sedlar, J. and Tjernström, M.: Clouds, warm air, and a climate cooling signal over the summer Arctic, *Geophys.
539 Res. Lett.*, 44(2), 1095–1103, doi:10.1002/2016GL071959, 2017.

540 Serreze, M. C. and Francis, J. A.: The arctic amplification debate, *Clim. Change*, 76(3–4), 241–264,
541 doi:10.1007/s10584-005-9017-y, 2006.

542 Simmonds, I.: Comparing and contrasting the behaviour of Arctic and Antarctic sea ice over the 35 year period

543 1979-2013, *Ann. Glaciol.*, 56(69), 18–28, doi:10.3189/2015AoG69A909, 2015.

544 [Simmonds, I. and Li, M.: Trends and variability in polar sea ice, global atmospheric circulations, and](#)
545 [baroclinicity, *Ann. N. Y. Acad. Sci.*, doi:10.1111/nyas.14673, 2021.](#)

546 Sotiropoulou, G., Sedlar, J., Tjernström, M., Shupe, M. D., Brooks, I. M. and Persson, P. O. G.: The
547 thermodynamic structure of summer Arctic stratocumulus and the dynamic coupling to the surface, *Atmos.*
548 *Chem. Phys.*, 14(22), 12573–12592, doi:10.5194/acp-14-12573-2014, 2014.

549 Tang, Q., Zhang, X., Yang, X. and Francis, J. A.: Cold winter extremes in northern continents linked to Arctic
550 sea ice loss, *Environ. Res. Lett.*, doi:10.1088/1748-9326/8/1/014036, 2013.

551 Tjernström, M. and Graverson, R. G.: The vertical structure of the lower Arctic troposphere analysed from
552 observations and the ERA-40 reanalysis, *Q. J. R. Meteorol. Soc.*, 135(639), 431–443, doi:10.1002/qj.380, 2009.

553 Tjernström, M., Birch, C. E., Brooks, I. M., Shupe, M. D., Persson, P. O. G., Sedlar, J., Mauritsen, T., Leck, C.,
554 Paatero, J., Szczodrak, M. and Wheeler, C. R.: Meteorological conditions in the central Arctic summer during
555 the Arctic Summer Cloud Ocean Study (ASCOS), *Atmos. Chem. Phys.*, 12(15), 6863–6889, doi:10.5194/acp-
556 12-6863-2012, 2012.

557 Tjernström, M., Shupe, M. D., Brooks, I. M., Persson, P. O. G., Prytherch, J., Salisbury, D. J., Sedlar, J.,
558 Achtert, P., Brooks, B. J., Johnston, P. E., Sotiropoulou, G. and Wolfe, D.: Warm-air advection, air mass
559 transformation and fog causes rapid ice melt, *Geophys. Res. Lett.*, 42(13), 5594–5602,
560 doi:10.1002/2015GL064373, 2015.

561 Tjernström, M., Shupe, M. D., Brooks, I. M., Achtert, P., Prytherch, J. and Sedlar, J.: Arctic summer airmass
562 transformation, surface inversions, and the surface energy budget, *J. Clim.*, 32(3), 769–789, doi:10.1175/JCLI-
563 D-18-0216.1, 2019.

564 Woods, C. and Caballero, R.: The role of moist intrusions in winter arctic warming and sea ice decline, *J. Clim.*,
565 29(12), 4473–4485, doi:10.1175/JCLI-D-15-0773.1, 2016.

566 Woods, C., Caballero, R. and Svensson, G.: Large-scale circulation associated with moisture intrusions into the
567 Arctic during winter, *Geophys. Res. Lett.*, 40(17), 4717–4721, doi:10.1002/grl.50912, 2013.

568 You, C., Tjernström, M. and Devasthale, A.: Warm-Air Advection Over Melting Sea-Ice: A Lagrangian Case
569 Study, *Boundary-Layer Meteorol.*, doi:10.1007/s10546-020-00590-1, 2020.

570 You, C., Tjernström, M. and Devasthale, A.: Eulerian and Lagrangian views of warm and moist air intrusions
571 into summer Arctic, *Atmos. Res.*, 256, doi:10.1016/j.atmosres.2021.105586, 2021.

572

573

574 Table 1. Regional averaged F_{sh} , F_{lh} , F_{sw} , F_{lw} and F_{total} in Kara, Laptev, East Siberian and
 575 Beaufort Sea sector. The unit is $W m^{-2}$ for all variables. Statistically significant positive values
 576 are in bold.

Sea sector	Barents	Kara	Laptev	East Siberian	Chukchi	Beaufort
F_{sh}	28.85±16.73	8.92±13.08	3.17±6.53	6.72±7.77	13.55±10.87	5.93 ±8.14
F_{lh}	10.05±9.83	0.65±6.58	-0.39±2.19	0.55±2.56	1.56±4.02	0.34±2.19
F_{sw}	-0.024±0.59	-0.077±0.40	-0.029±0.40	-0.16±0.47	-0.095±0.97	-0.077±0.9
F_{lw}	15.99±14.34	16.51±9.93	5.92±10.88	15.42±11.16	21.77±10.30	17.45±10.51
F_{total}	54.86±34.41	26.01±25.32	8.67±13.81	22.52±15.08	36.78±16.27	23.65±14.85

577

578 Table 2. Number of WaMAIs with boundary layer energy budget pattern of category RAD
 579 (radiation-dominated), TBL (turbulence-dominated), TCD (turbulence-dominated with cold
 580 dome) and INV (lifting temperature inversion), over melting (Barents) and frozen (Laptev,
 581 East Siberian, Chukchi and Beaufort) sea sectors.

Formatted: Space Before: 6 pt

Sea sector	Melting			Frozen
	RAD	TBL	TCD	INV
Number	9	45	33	131

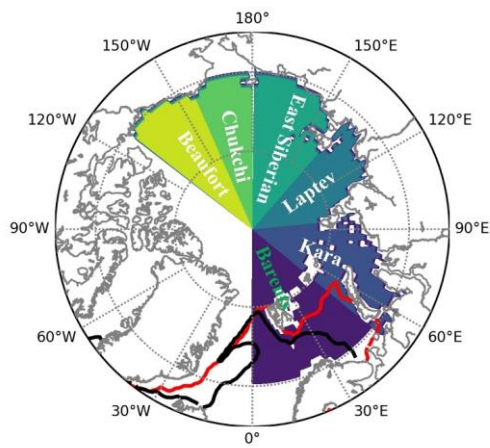
582 Table 3. Averaged F_{sh} , F_{lh} , F_{sw} , F_{lw} , TCLW (from bottom to h_{tz} ; $g m^{-2}$) and large-scale
 583 convergence (CONV; $10^{-5} kg m^{-2} s^{-1}$) from category TBL and category RAD. Statistically
 584 significant positive values are in bold.

Formatted: Space Before: 6 pt

Formatted: English (United Kingdom)

	Category RAD	Category TBL	Category TCD
F_{sw}	-0.0094±0.047	-0.00035±0.0013	-0.0050±0.035
F_{lw}	31.49±13.96	34.61±18.71	35.46±13.10
F_{sh}	40.99±28.27	72.58±40.21	9.77±23.08
F_{lh}	17.43±15.42	24.79±23.80	1.02±8.16
TCLW	96.78±53.31	83.11±54.27	30.13±31.89
CONV	17.19±174.89	236.05±225.90	115.00±230.01
Wind Shear	0.019±0.0061	0.026±0.008	0.02±0.011

585
586
587

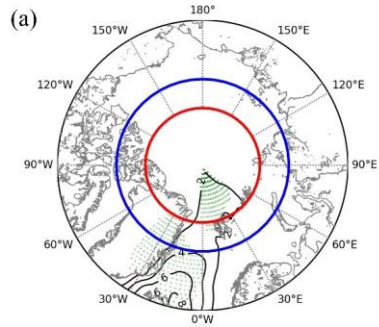


588

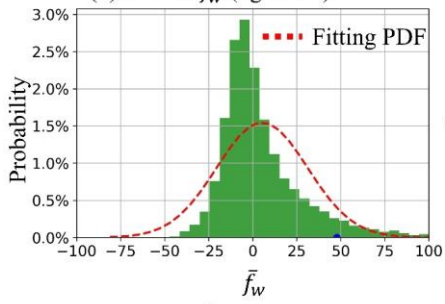
589 Figure 1. Locations of siesix sea sectors discussed in this paper, the Barents, Kara, Laptev,
590 East Siberian, Chukchi and Beaufort Sea sectors. Black line is the mean March sea-ice edge
591 in 1979 and red line is the mean March sea-ice edge in 2015 when the minimum winter sea
592 ice cover was recorded.

593

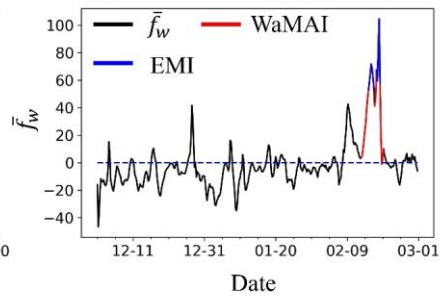
Formatted: Left, Line spacing: Multiple 1.07 li



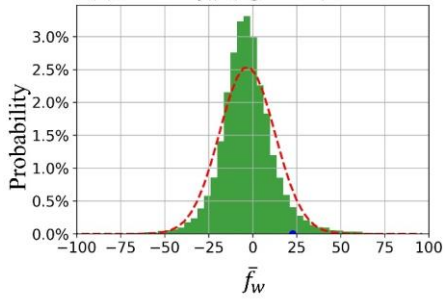
(b) PDF of \bar{f}_w ($\text{kg m}^{-1}\text{s}^{-1}$)



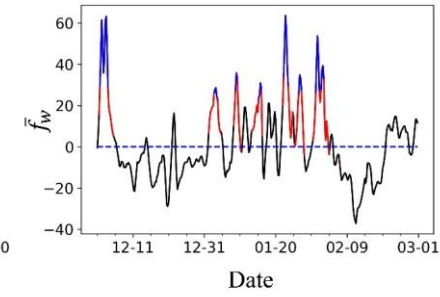
(c) Time Series of \bar{f}_w ($\text{kg m}^{-1}\text{s}^{-1}$)

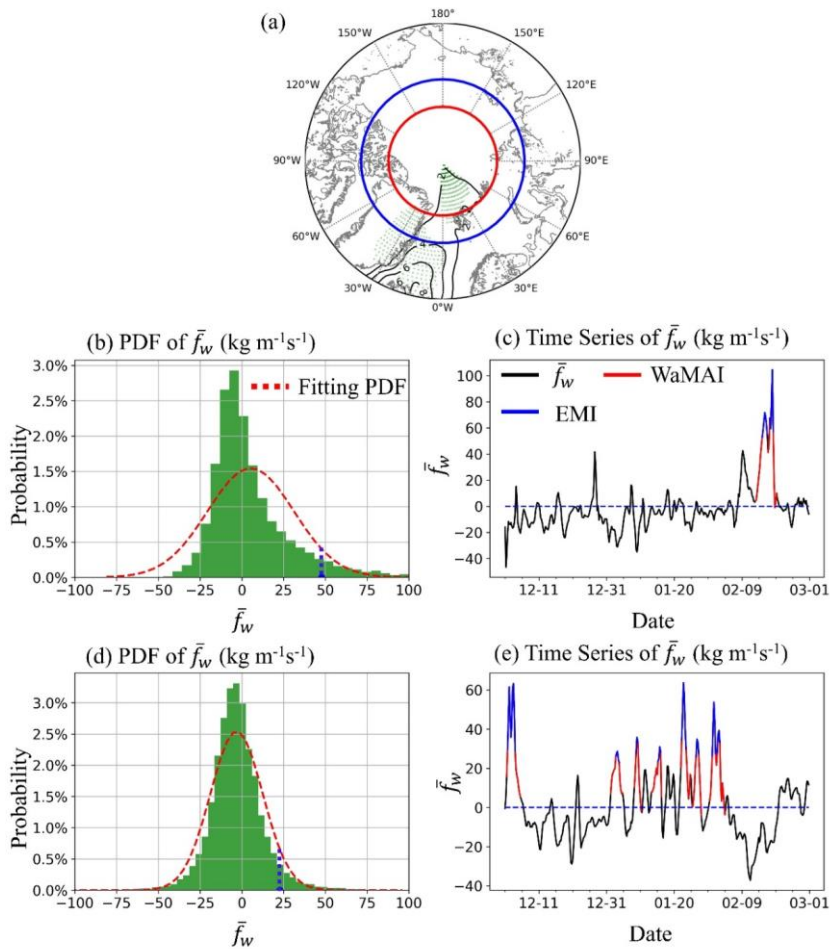


(d) PDF of \bar{f}_w ($\text{kg m}^{-1}\text{s}^{-1}$)



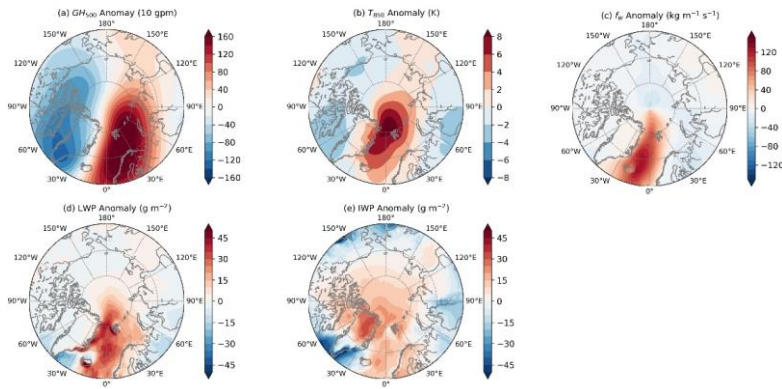
(e) Time Series of \bar{f}_w ($\text{kg m}^{-1}\text{s}^{-1}$)



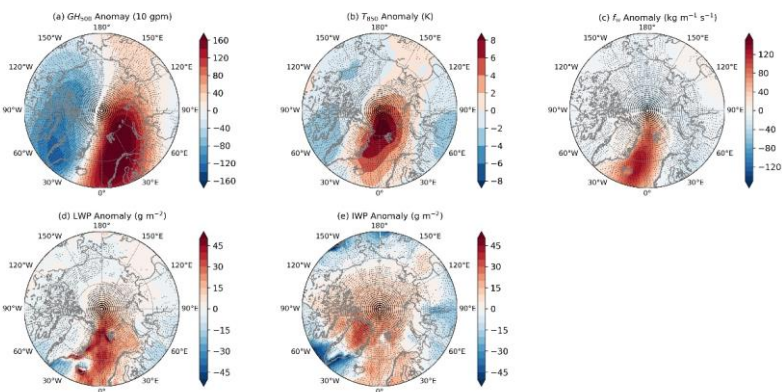


595
 596 Figure 2. (a) Contours of the linear correlation between local f_w and normalized SIC anomalies
 597 (multiplied by -1), defined as the anomaly divided by its standard deviation, for the winter
 598 ~~month~~ months (DJF) over the Barents Sea. The stippling indicates statistical significance at
 599 the $p < 0.05$ level for the Student's t test. Red line is the latitude of 80°N where the trajectories
 600 over the Barents Sea are launched, while blue line is the latitude of 75°N where the trajectories
 601 are launched over the sea sectors of Kara, Laptev, East Siberian, Chukchi and Beaufort; (b)
 602 and (d) show the Probability Distribution Function of f_w over the Barents and Beaufort Sea,
 603 respectively, with the 95-percentile marked as a blue ~~dash~~dash line; (c) and (e) are the time series
 604 of f_w over the Barents Sea and Beaufort Sea in 1980, respectively, with WaMAI highlighted
 605 in red and EMIs highlighted in blue.

606
607
608
609
610
611
612
613
614



615



616

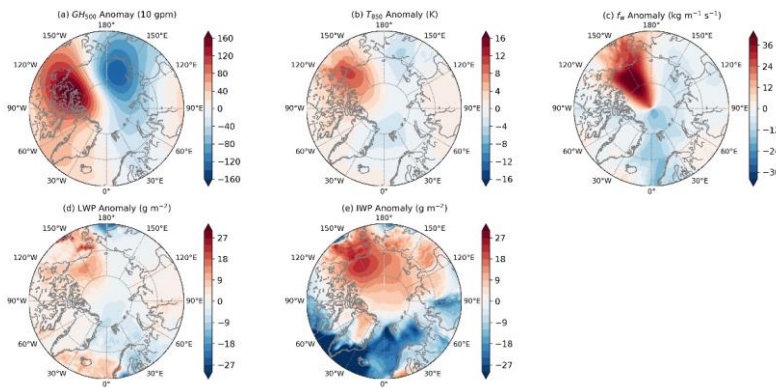
617 Figure 3. Composite ERA5 anomalies of (a) 500-hPa GH (10 gpm), (b) 850-hPa temperature
 618 (K), (c) northward water-vapor flux ($kgm^{-1}s^{-1}$), (d) liquid water path ($g m^{-2}$), and (e) ice
 619 water path for all EMIs over the Barents Sea, during 1979~2018 winters. The stippling
 620 indicates statistical significance at the $p < 0.01$ level from a Student's t test.

Formatted: Justified

Formatted: Font: +Body (Calibri), 11 pt

Formatted: Font: Times New Roman, 12 pt

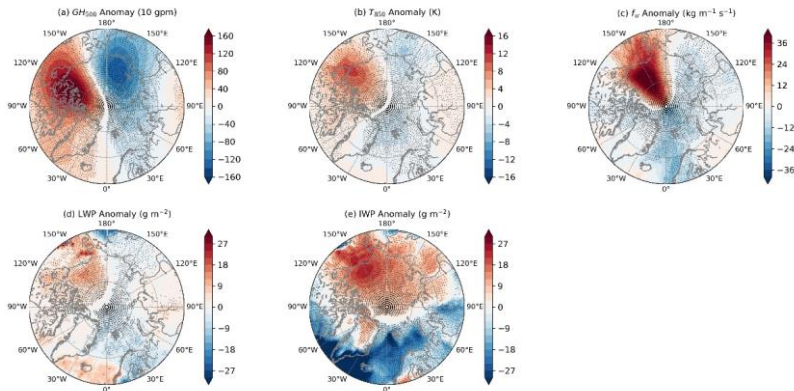
621



622

623

624



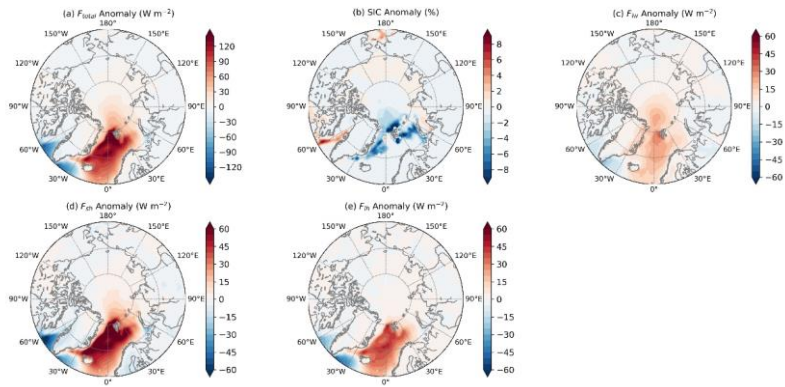
625

626 Figure 4. Composite ERA5 anomalies of (a) 500-hPa GH (10 gpm), (b) 850-hPa temperature
 627 (K), (c) northward water-vapor flux ($kgm^{-1}s^{-1}$), (d) liquid water path ($g m^{-2}$), and (e) ice
 628 water path for all EMIs over the Beaufort Sea, during 1979~2018 winters. The stippling
 629 indicates statistical significance at the $p < 0.01$ level from a Student's t test.

Formatted: Justified

Formatted: Font color: Custom Color(RGB(26,26,26)),
 Pattern: Clear (White)

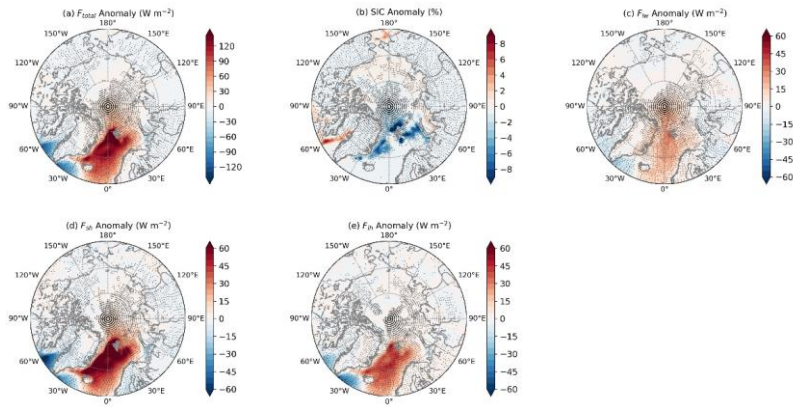
630



631

632

633



634

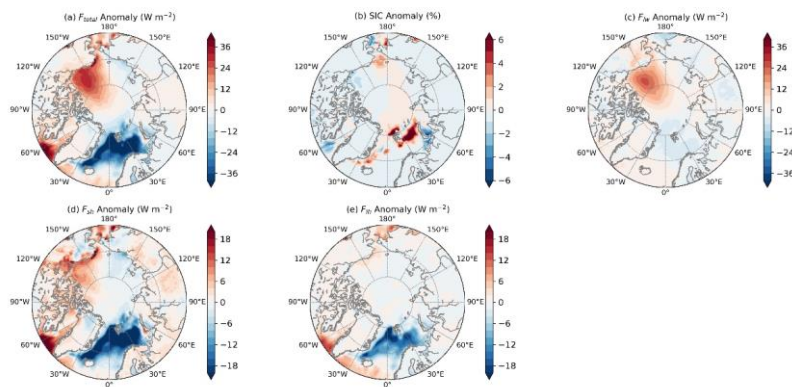
635

636 Figure 5. Composite ERA5 anomalies of (a) total surface energy (W m^{-2}), (b) sea ice
 637 concentration (%), (c) surface thermal net irradiance (W m^{-2}), (d) surface sensible heat flux (W
 638 m^{-2}) and (e) surface latent heat flux (W m^{-2}) for all EMIs over the Barents Sea, during
 639 1979~2018 winter. The stippling indicates statistical significance at the $p < 0.01$ level from a
 640 Student's t test.

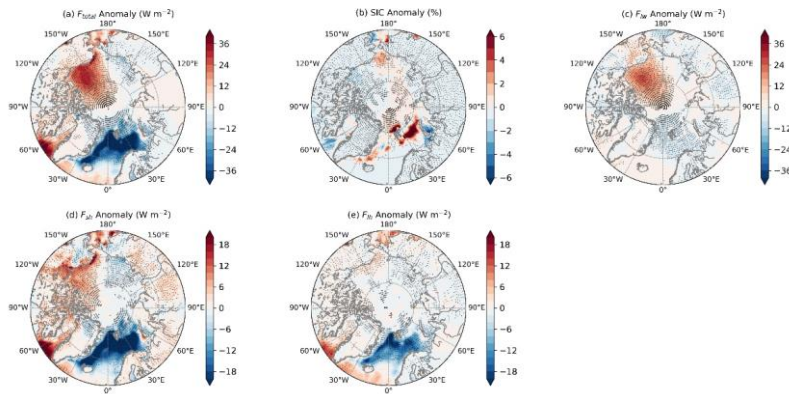
Formatted: Justified

641

Formatted: Font: +Body (Calibri), 11 pt



642



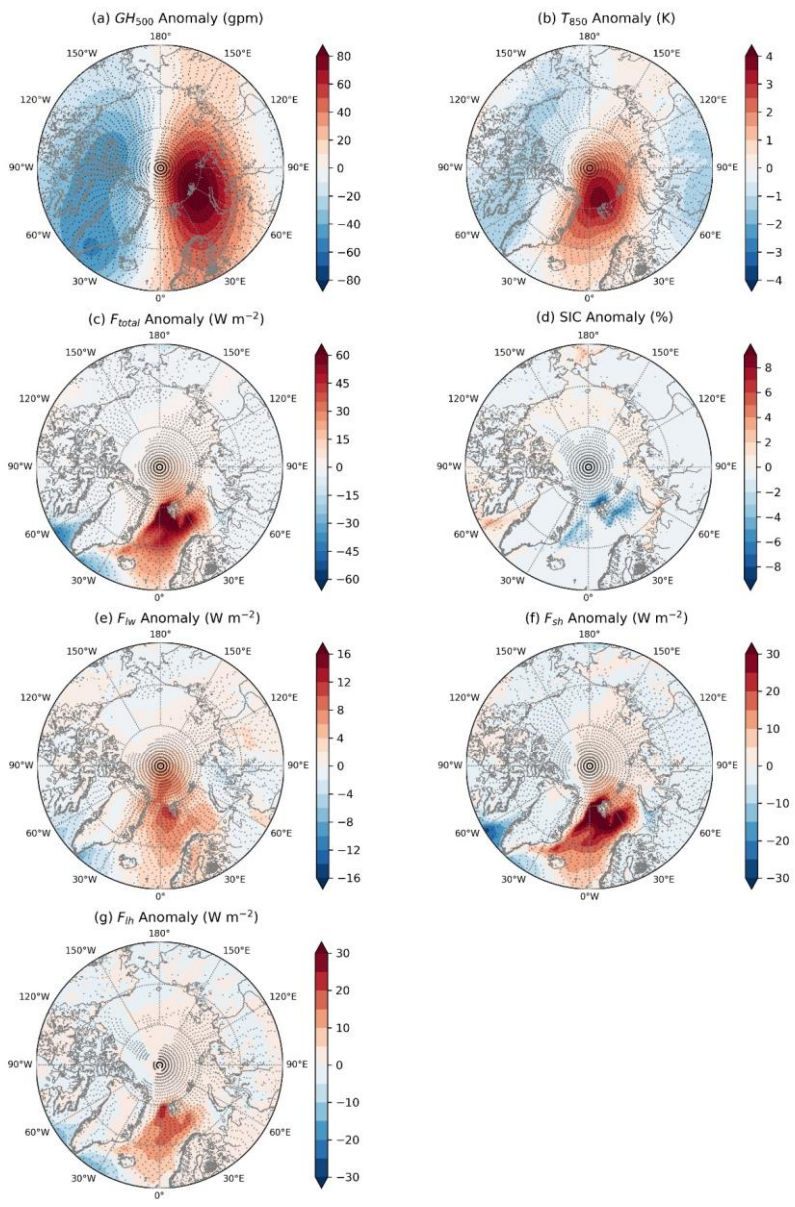
643

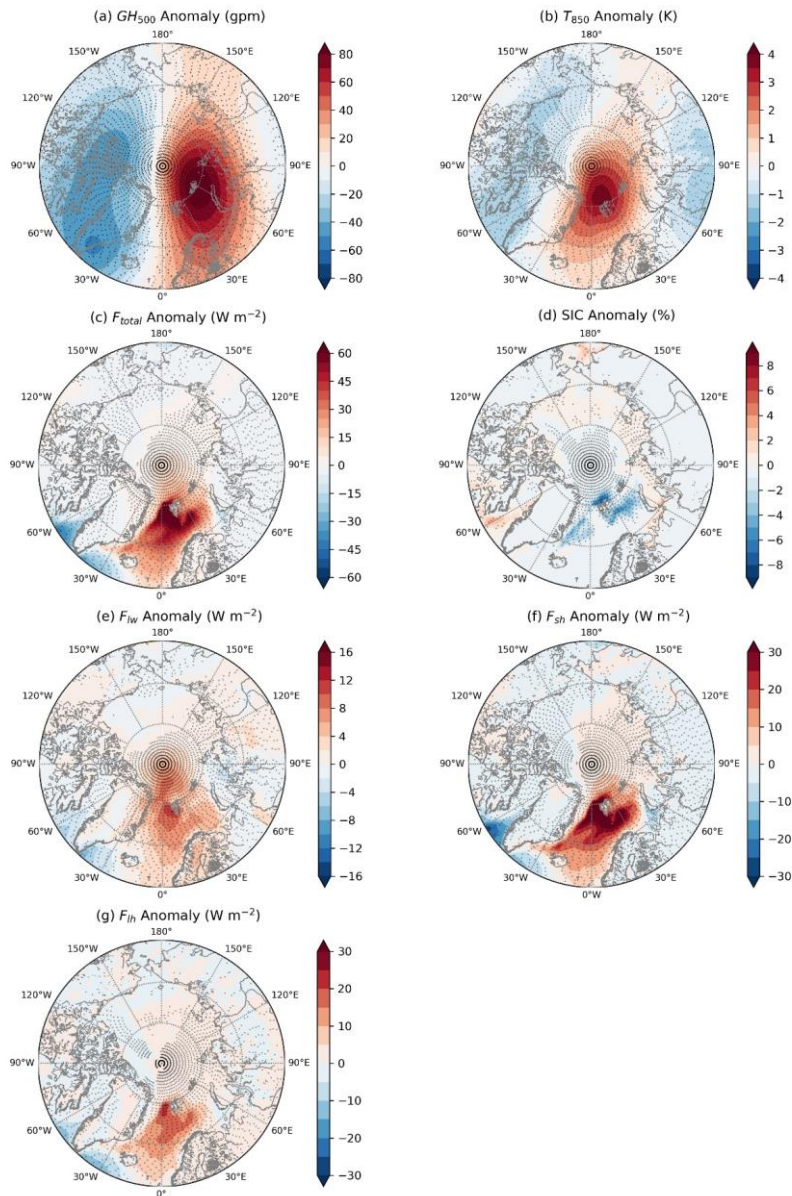
644 Figure 6. Composite ERA5 anomalies of (a) total surface energy (W m^{-2}), (b) sea ice
 645 concentration (%), (c) surface thermal net irradiance (W m^{-2}), (d) surface sensible heat flux (W
 646 m^{-2}) and (e) surface latent heat flux (W m^{-2}) for all EMIs over the Beaufort Sea, during
 647 1979~2018 winter. Noted that the color-bars here are different than those in figure 5. The
 648 stippling indicates statistical significance at the $p < 0.01$ level from a Student's t test.

649

Formatted: Justified

Formatted: Font: +Body (Calibri), 11 pt



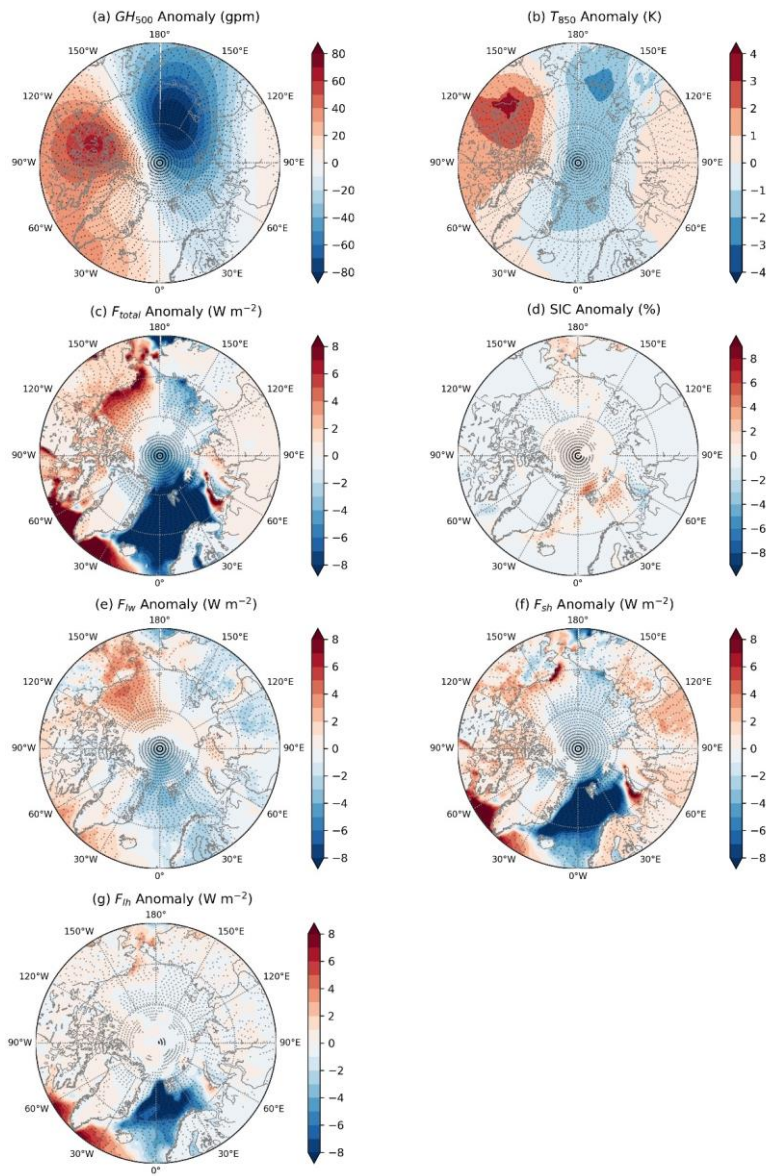


651

652 Figure 7. Anomalies of (a) 500-hPa geopotential height (gpm), (b) 850-hPa temperature (K),
 653 (c) F_{total} , (d) SIC, (e) F_{lw} , (f) F_{sh} , and (g) F_{lh} from linear regressions against daily \bar{f}_w time
 654 series over the Barents Sea. The stippling indicates statistical significance at the $p < 0.05$ level
 655 from a Student's t test.

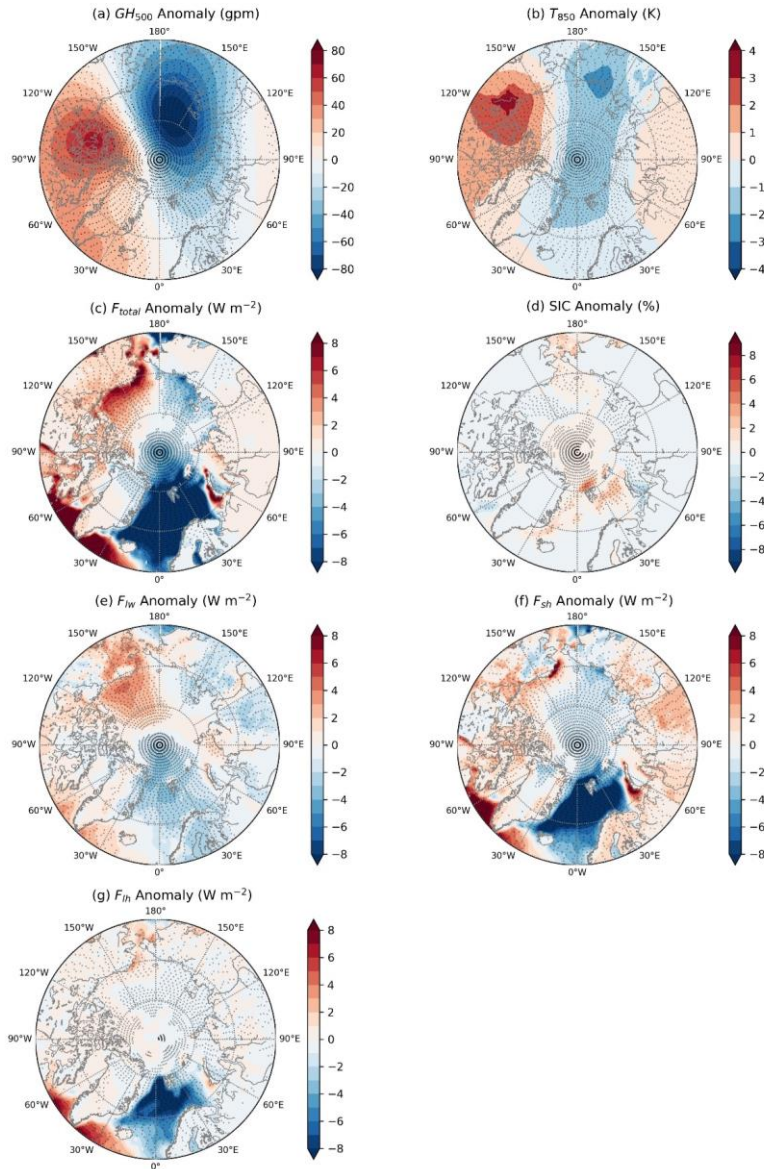
656

657



658

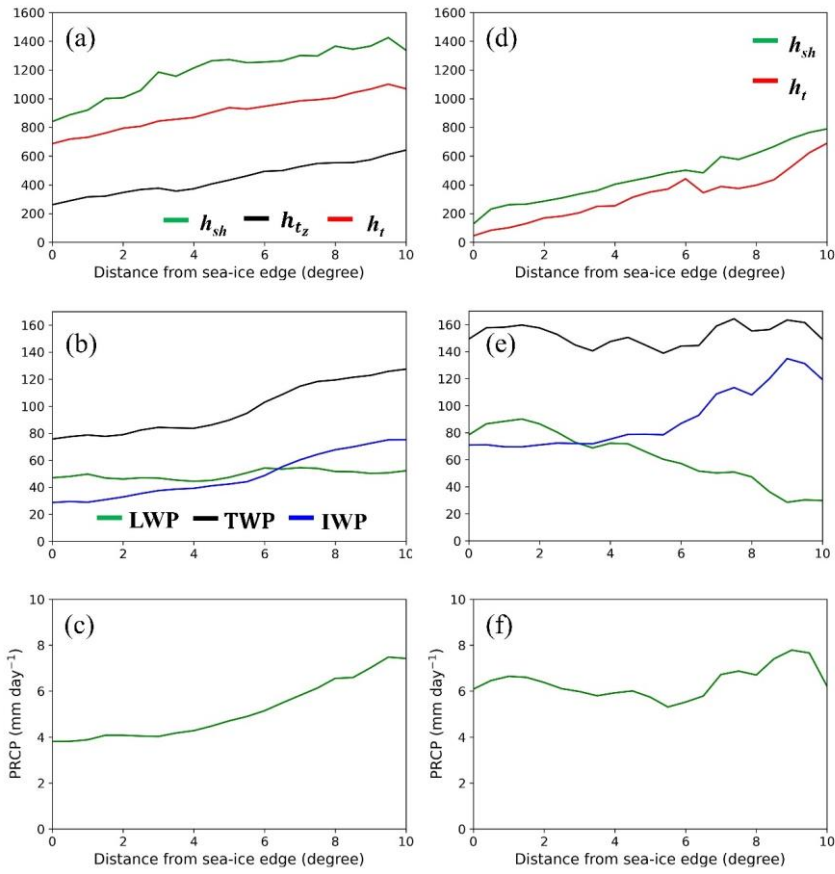
659

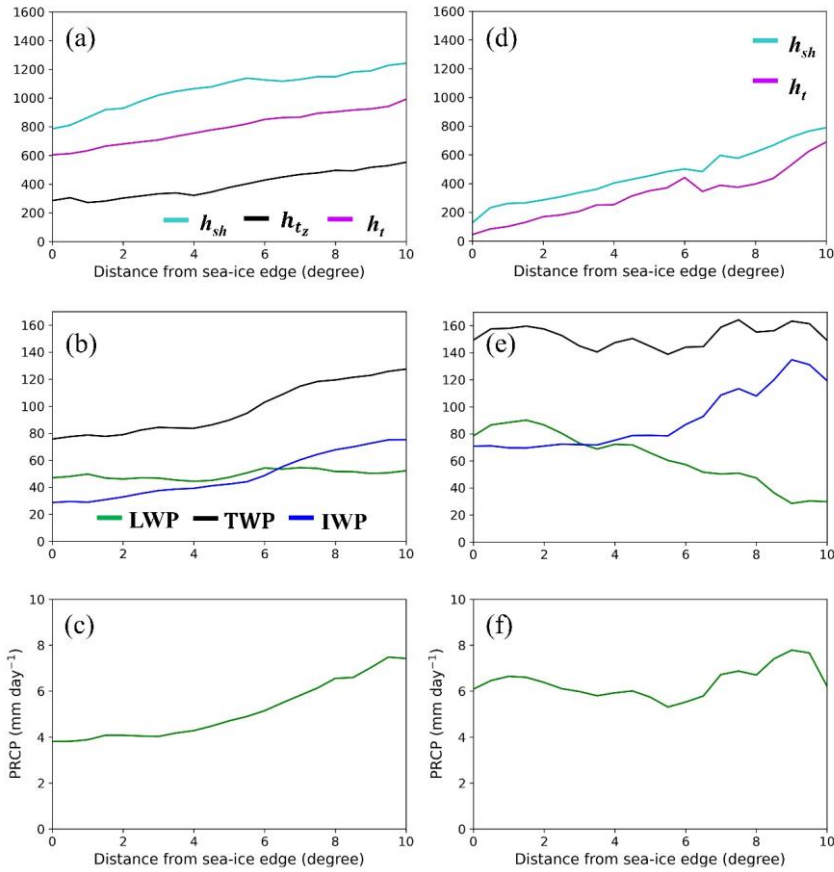


661

662 Figure 8. Anomalies of (a) 500-hPa geopotential height (gpm), (b) 850-hPa temperature (K),
 663 (c) F_{total} , (d) SIC, (e) F_{lw} , (f) F_{sh} , and (g) F_{lh} from linear regressions against daily \bar{f}_w time
 664 series over the Beaufort Sea. The stippling indicates statistical significance at the $p < 0.05$
 665 level from a Student's t test.

Formatted: Font color: Custom Color(26,26,26),
 Pattern: Clear (White)

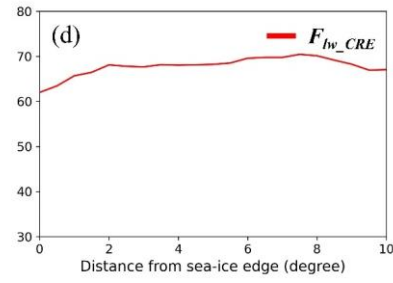
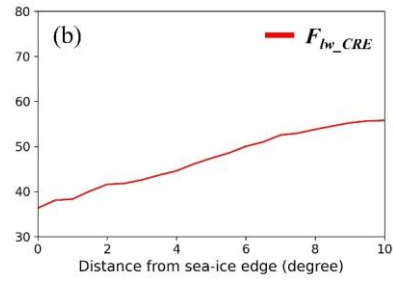
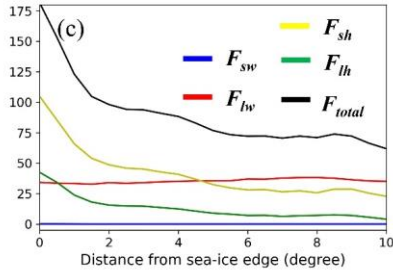
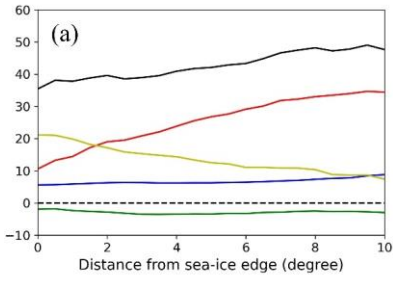




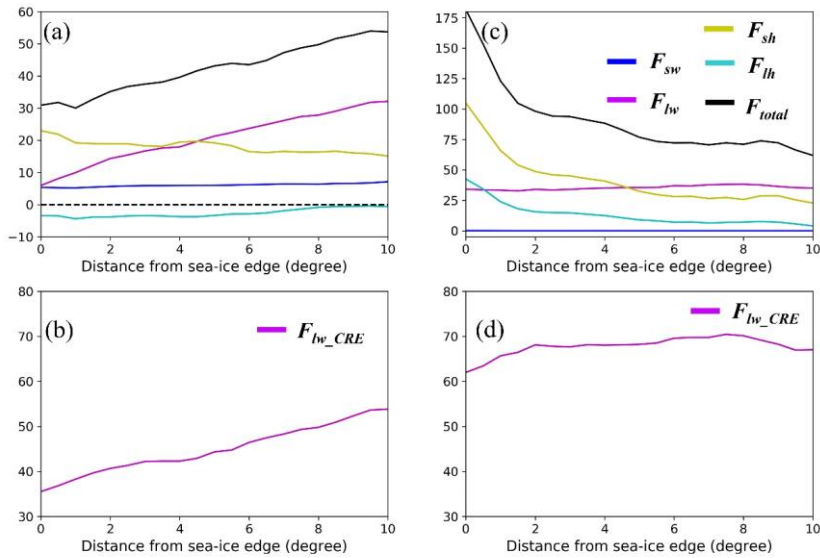
669
670

671 Figure 9: Average variation of (a) the height to the maximum specific humidity (h_{sh}),
 672 temperature gradient (h_{tz} ; m) and temperature (h_t); (b) liquid water path (LWP; g m^{-2}), ice
 673 water path (IWP; g m^{-2}) and total water path (TWP; g m^{-2}); (c) precipitation rate (PRCP; mm day^{-1}),
 674 with the downstream northward distance from sea-ice edge, along the WaMAI
 675 trajectories over the Barents Sea. ~~Noted that the distance here is only measured in the~~
 676 ~~meridional direction.~~ (d) (e) (f) are the counterparts of (a)(b)(c) over the frozen seas. Note that
 677 this is not necessarily the distance travelled, since WaMAIs do not need to travel due northward.

Formatted: Justified



680



681

682 Figure 10. ~~Plots showing~~ the average meridional ~~change~~ evolution in the anomalies of (a) the
683 sum (F_{total} , $W m^{-2}$; black) and individual surface fluxes of sensible heat (F_{sh} , $W m^{-2}$; yellow), latent
684 heat (F_{lh} , $W m^{-2}$; ~~green~~ cyan), net longwave irradiance (F_{lw} , $W m^{-2}$; ~~red~~ magenta) and net shortwave
685 irradiance (F_{sw} , $W m^{-2}$; blue) along the trajectories. (b) shows the cloud radiative effect by longwave
686 (F_{lw_CRE} ; ~~red~~ magenta) over the Barents Sea. (c)(d) are the counterparts of (a)(b) over the frozen seas.
687 ~~Noted that the X axis (distance from sea ice edge) here is only measured in the meridional~~
688 ~~direction.~~

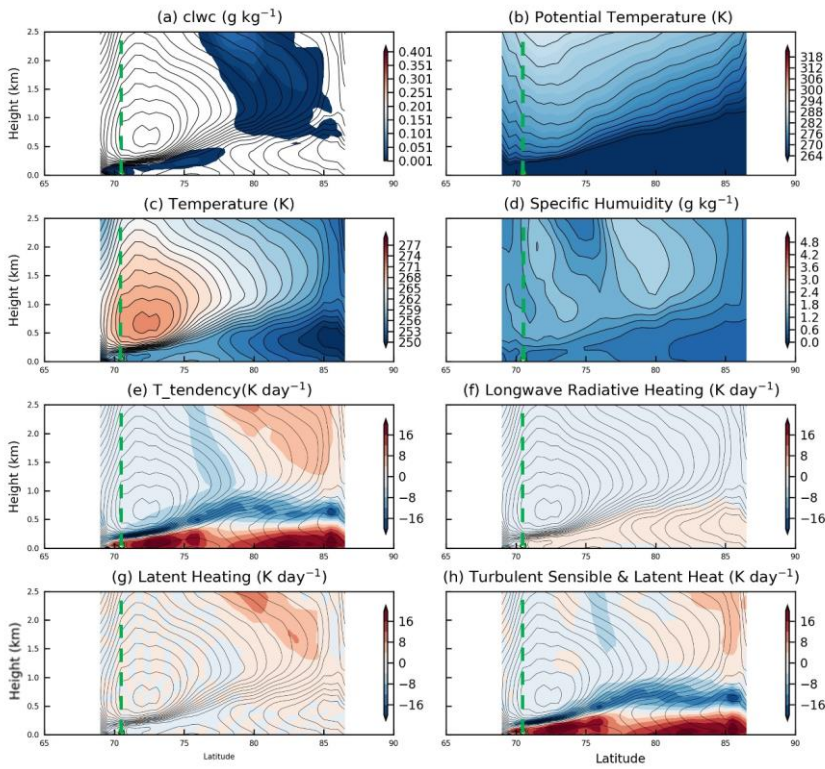
Formatted: Font: 11 pt

689

690

691

692



693

694

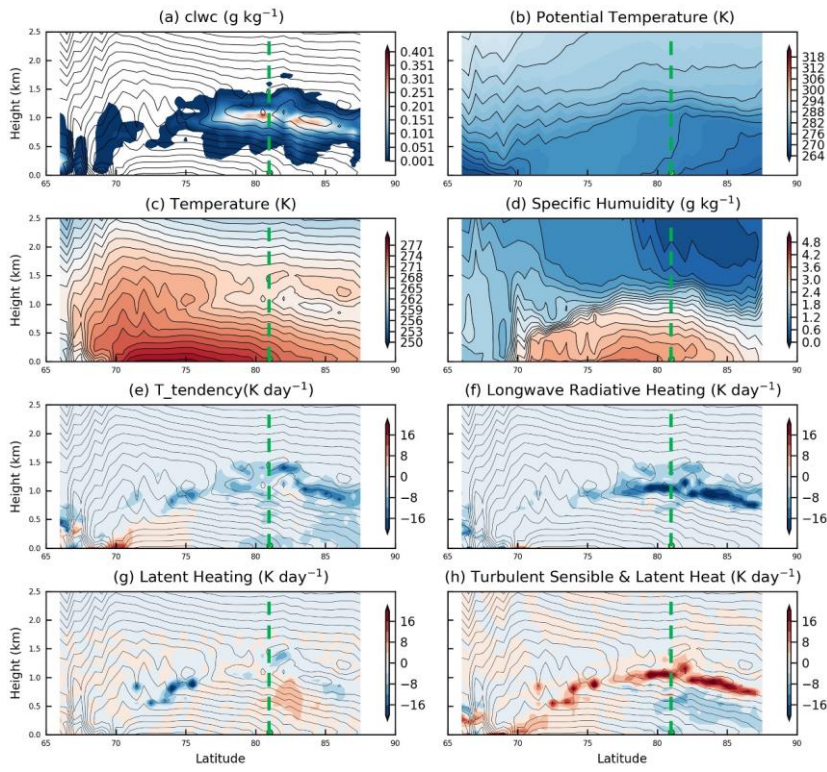
695

696 Figure 11. Latitude-height cross-section of (a) cloud liquid water concentration (g kg^{-1}), (b) potential
 697 potential temperature (K), (c) temperature (K), (d) specific humidity (g kg^{-1}), (e) temperature tendency due
 698 to model physics (K day^{-1}), (f) longwave radiative heating (K day^{-1}), (g) latent heating (K day^{-1}) and (h)
 699 turbulent heating (K day^{-1}), interpolated from ERA5 along trajectories of one
 700 selected WaMAI from category INV. The green dash lines mark the location of ice-edge. See the text
 701 for a detailed discussion.

702

703

704



705

706

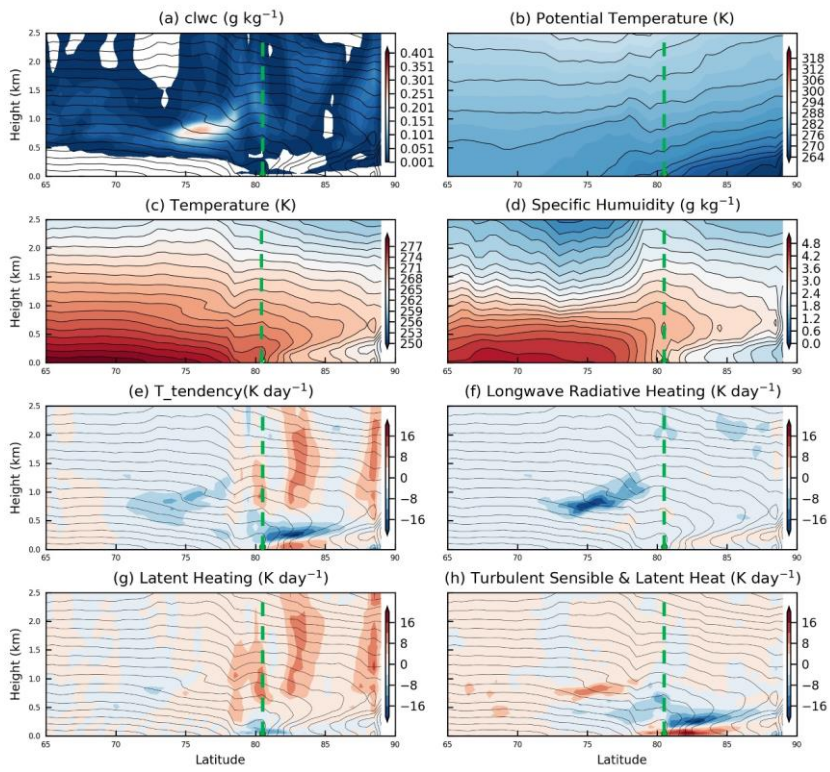
707 Figure 12. Same as figure 13.11 but for a selected radiation-dominated WaMAI.

708

709

710

711

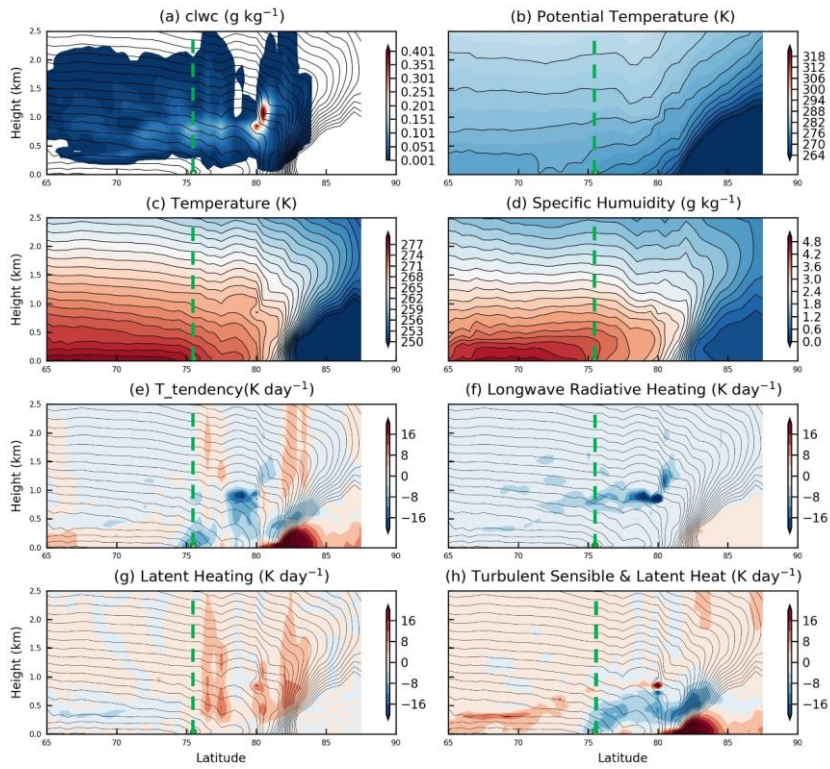


712

713 Figure 13. Same as figure 1011 but for a selected turbulence-dominated WaMAI.

714

715

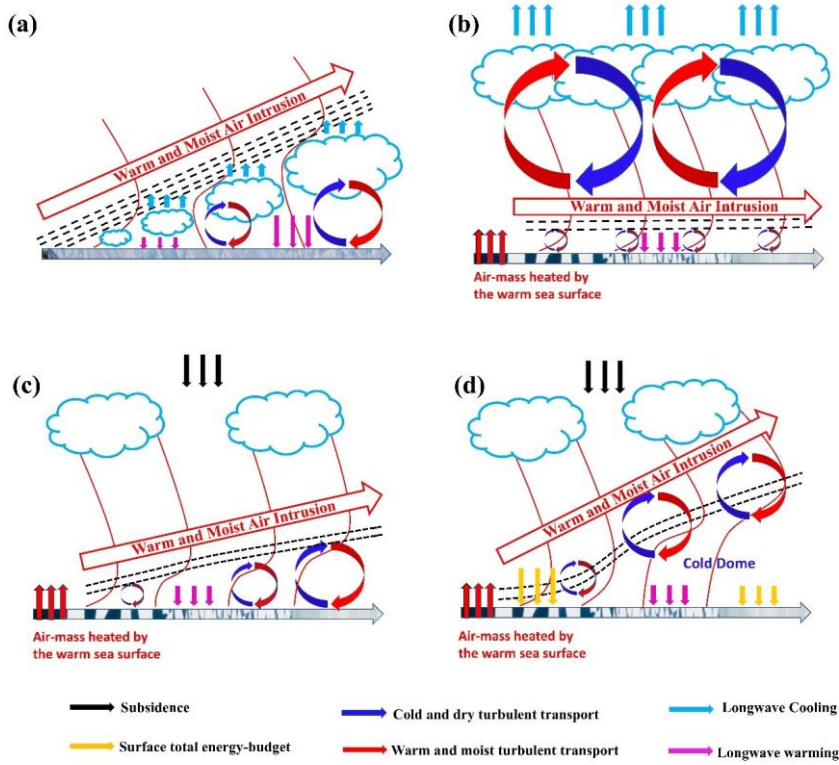


716

717

718 Figure 14. Same as figure 1011 but for a selected turbulence-dominated WaMAI with cold
719 dome.

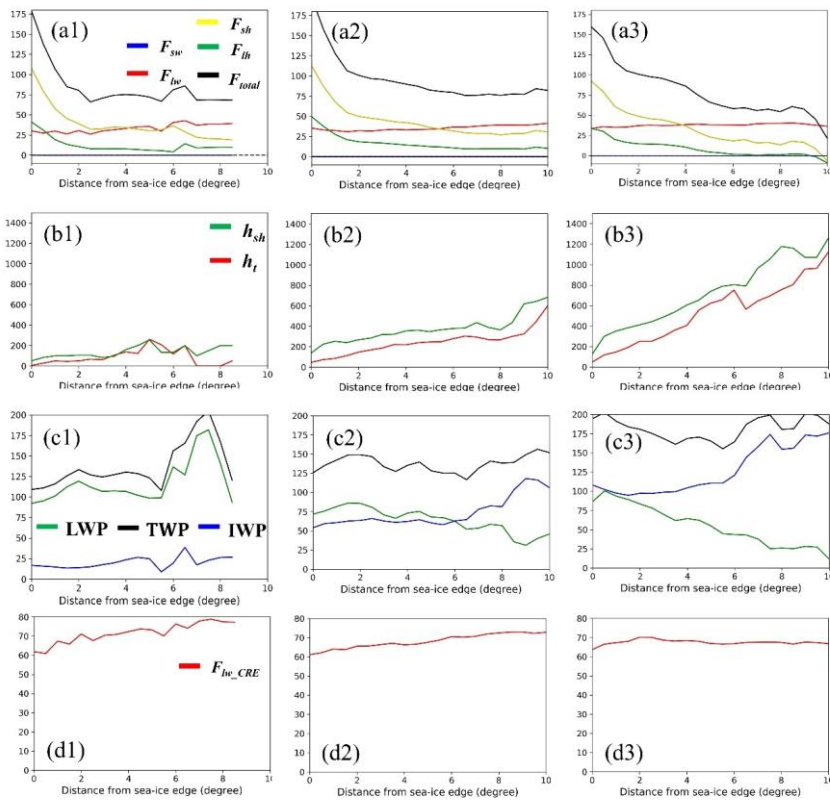
720



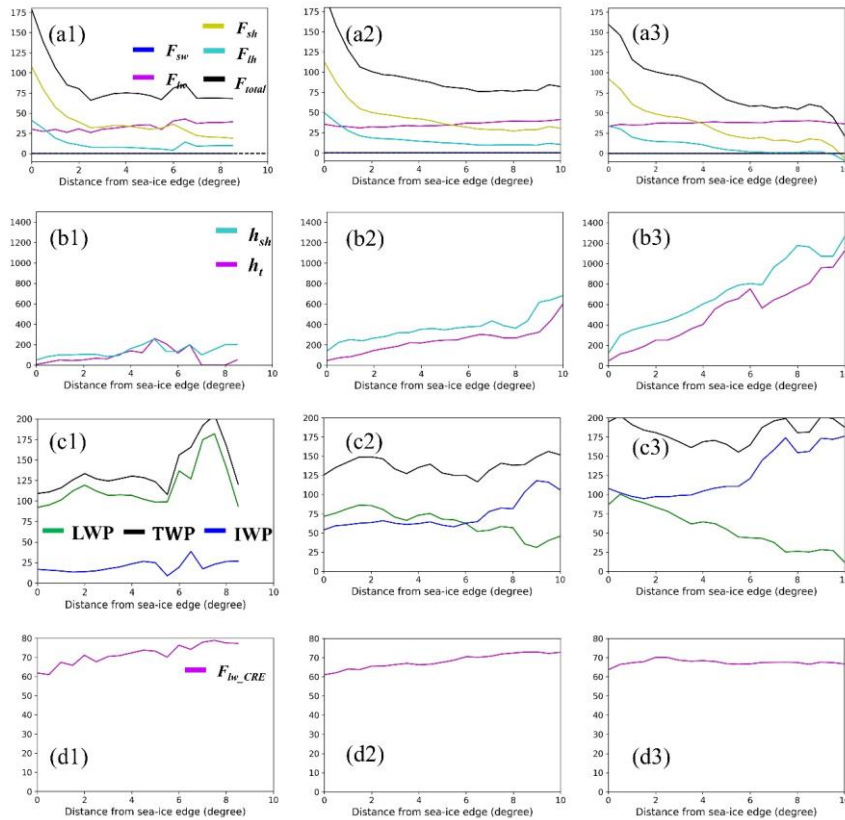
723 Figure 15. Concept graph of WaMAI from category (a) INV, (b) radiation-dominated
 724 WaMAI, (c) turbulence-dominated WaMAI, (d) turbulence-dominated WaMAI with cold
 725 dome. The red lines in (a)(b)(c) are temperature or humidity profiles. Red arrows represent
 726 the WaMAIs. The horizontal arrows represent the Arctic surface with frozen or melting sea-
 727 ice. Black lines represent inversions.

Formatted: Font: Times New Roman, 12 pt

736
737
738



739
740



741
 742 Figure 16. Average variation of (a1) the sum (F_{total} , $W m^{-2}$; black) and individual surface fluxes
 743 of sensible heat (F_{sh} , $W m^{-2}$; yellow), latent heat (F_{lh} , $W m^{-2}$; ~~green~~cyan), net longwave
 744 irradiance (F_{lw} , $W m^{-2}$; ~~red~~magenta) and net shortwave irradiance (F_{sw} , $W m^{-2}$; blue); (b1) the
 745 height to the maximum specific humidity (h_{sh}) and temperature (h_t); (c1) liquid water path
 746 (LWP; $g m^{-2}$), ice water path (IWP; $g m^{-2}$) and total water path (TWP; $g m^{-2}$); (d1) the cloud
 747 radiative effect by longwave (F_{lw_CRE} ; ~~red~~magenta), with the downstream northward distance
 748 from sea-ice edge, along the trajectory of WaMAI in category of RAD over the Barents Sea.
 749 (a2)(b2)(c2)(d2) ((a3)(b3)(c3)(d3)) are the same but for WaMAIs in category of TBL (TCD).

750
 751
 752